

Acta Crystallographica Section A

**Foundations of
Crystallography**

ISSN 0108-7673

Editors: **S. J. L. Billinge and J. Miao**

Periodic entanglement I: networks from hyperbolic reticulations

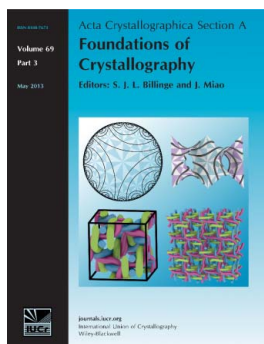
Myfanwy E. Evans, Vanessa Robins and Stephen T. Hyde

Acta Cryst. (2013). **A69**, 241–261

Copyright © International Union of Crystallography

Author(s) of this paper may load this reprint on their own web site or institutional repository provided that this cover page is retained. Republication of this article or its storage in electronic databases other than as specified above is not permitted without prior permission in writing from the IUCr.

For further information see <http://journals.iucr.org/services/authorrights.html>



Acta Crystallographica Section A: Foundations of Crystallography covers theoretical and fundamental aspects of the structure of matter. The journal is the prime forum for research in diffraction physics and the theory of crystallographic structure determination by diffraction methods using X-rays, neutrons and electrons. The structures include periodic and aperiodic crystals, and non-periodic disordered materials, and the corresponding Bragg, satellite and diffuse scattering, thermal motion and symmetry aspects. Spatial resolutions range from the subatomic domain in charge-density studies to nanodimensional imperfections such as dislocations and twin walls. The chemistry encompasses metals, alloys, and inorganic, organic and biological materials. Structure prediction and properties such as the theory of phase transformations are also covered.

Crystallography Journals **Online** is available from journals.iucr.org

Periodic entanglement I: networks from hyperbolic reticulations

Myfanwy E. Evans,^{a,b*} Vanessa Robins^a and Stephen T. Hyde^a

^aDepartment of Applied Mathematics, Research School of Physics, Australian National University, Canberra, ACT 0200, Australia, and ^bInstitut für Theoretische Physik, Friedrich-Alexander Universität Erlangen-Nürnberg, Germany. Correspondence e-mail: myfanwy.e.evans@physik.uni-erlangen.de

High-symmetry free tilings of the two-dimensional hyperbolic plane (\mathbb{H}^2) can be projected to genus-3 3-periodic minimal surfaces (TPMSs). The three-dimensional patterns that arise from this construction typically consist of multiple catenated nets. This paper presents a construction technique and limited catalogue of such entangled structures, that emerge from the simplest examples of regular ribbon tilings of the hyperbolic plane *via* projection onto four genus-3 TPMSs: the *P*, *D*, *G*(yroid) and *H* surfaces. The entanglements of these patterns are explored and partially characterized using tools from *TOPOS*, *GAVROG* and a new tightening algorithm.

© 2013 International Union of Crystallography
Printed in Singapore – all rights reserved

1. Introduction

The interpenetration of multiple networks (or nets) is a challenging issue from a geometric perspective. The topic is also one of relevance to materials science. Although they are difficult to characterize mathematically, or indeed identify in chemical systems, their importance has long been recognized. Alexander Wells, who pioneered the systematic study of nets, recognized the potential importance of multiple nets and discussed some examples in detail (Wells, 1977). They are often encountered in typically highly porous metal–organic frameworks (MOFs), whose various catenation types have been the subject of a number of studies (Batten & Robson, 1998; Chen *et al.*, 2001; Carlucci *et al.*, 2003; Blatov *et al.*, 2004; Baburin *et al.*, 2005; Eon, 2006; Blatov, 2006; Blatov & Proserpio, 2009; Alexandrov *et al.*, 2011; Eon *et al.*, 2012). They are also found in bicontinuous liquid crystalline mesophases and related mesoporous tricontinuous inorganic derivatives (Han *et al.*, 2009). Novel ‘polycontinuous’ open foam-like patterns have also been formed starting from multiple nets (Hyde & Ramsden, 2000a; Hyde *et al.*, 2009; Schröder-Turk *et al.*, 2013).

We adopt the following definitions. First, a *graph* is a topological object without geometry, defined by points and their mutual connections *via* edges; *simple* graphs have no more than one edge between any vertex pair. We discuss here mostly infinite graphs, with an unbounded number of vertices and edges. An *embedding* of a graph is a geometric realization of that graph in a space, with assigned geometry (*e.g.* coordinates) for vertices and all edge points. The number of independent translation vectors of the graph embedding defines its periodicity: we are concerned here with 1-, 2- and 3-periodic graph embeddings. The number of edges that share a vertex characterizes the *degree* of that vertex; if all vertices have

equal degree (*e.g.* z), the graph and its embeddings have degree z . In concordance with graph theory, we understand a *k-connected* graph to mean that at least k vertices and their associated edges must be deleted from the graph to split it into more than a single disjoint graph. *Nets* are simple 3-connected graph embeddings (Beukemann & Klee, 1992; Klee, 2004).

In order to classify discrete groups of hyperbolic space, we adopt the *orbifold* concept, developed by Thurston (1980), which essentially describes all symmetry operations acting on a single asymmetric domain [a concept equally useful to two-dimensional plane groups in \mathbb{E}^2 (Conway & Huson, 2002)]. We use Conway’s (1992) orbifold nomenclature to describe the groups. For convenience, we classify orbifolds into classes determined by their symmetry operators (or, equivalently, the orbifold topology). Here we deal only with three classes. Coxeter orbifolds have a single mirror-line boundary and no internal centres of rotation symmetry (denoted by ‘ \star ’ symbols). Stellate orbifolds are free of reflection isometries and characterized by centres of rotation symmetry (whose orders build the orbifold symbol). Hat orbifolds contain features of both previous classes, with mirrors and rotation centres (not on mirror lines). (Like Euclidean space, hyperbolic space can also be symmetrically decorated with patterns containing translation and glide reflection isometries, denoted ‘ \circ ’ and ‘ \times ’, respectively.)

This paper and its companion (Evans *et al.*, 2013) are focused on (*en*)*tangled* graph embeddings, which are typically constituted of a number of disjoint components, wound around each other with varying degrees of mutual threading. A robust signature of entanglement is unsolved in general, though we develop in this paper an algorithmic approach that sheds some light on the issue. Identifying entanglement is related to the issue of identifying equivalent knots, a central concern of knot theory (Adams, 2004), though more complex.

Knots are (possibly) tangled embeddings of a topological loop; here we are interested in embeddings of a far broader class of graphs. We consider any pair of embeddings to be equivalent if they share the same entanglements (notwithstanding the associated difficulties in characterization of that entanglement). In mathematical language, that implies the embeddings are *ambient isotopic*, *i.e.* capable of being continuously transformed from one to the other such that distinct edges never share a common point in space, precluding edges from passing through each other. Embeddings that are not ambient isotopic, and have distinct entanglements, are distinct *isotopes* (Castle *et al.*, 2011).

This paper and its companion (Evans *et al.*, 2013) share a common approach to enumeration of entangled graph embeddings. Our technique relies on the possibility of embedding any graph in a two-dimensional (curved) surface (Lindsay, 1959). If that surface is a triply periodic minimal surface (TPMS), conventional Delaney–Dress tiling theory can be used to enumerate (crystalline) nets as reticulations of the TPMS to an arbitrary degree of complexity. This method simplifies somewhat the enumeration of nets embedded in three-dimensional Euclidean space (\mathbb{E}^3), translating that problem to the enumeration of TPMS tilings. The latter problem is solved by first finding symmetric tilings of the universal cover of the TPMS, namely the hyperbolic plane (\mathbb{H}^2). In order to project the \mathbb{H}^2 pattern to the TPMS, admissible hyperbolic patterns have isometries that are also isometries of the surface (*i.e.* symmetries of \mathbb{H}^2 , rather than \mathbb{E}^3) (Sadoc & Charvolin, 1989). We restrict allowed isometries to those that retain the full translational symmetries of the TPMS, thereby guaranteeing the construction of 3-periodic nets in \mathbb{E}^3 (Robins *et al.*, 2004a). This amounts to deducing all orbifolds whose associated groups are subgroups of $\star 246$ and supergroups of $\circ \circ \circ$. Admissible groups are listed in Robins *et al.* (2004a); we adopt the same numbering scheme for groups as listed there.

Patterns in the hyperbolic plane cannot be represented on a flat page without some distortion. We choose to draw \mathbb{H}^2 using the Poincaré disc model of \mathbb{H}^2 (Hilbert & Cohn-Vossen, 1952; Coxeter, 1947; Beardon, 1995).¹

The simplest TPMSs are the so-called genus-3 TPMSs (Hyde *et al.*, 1997). Among those, the cubic examples, Schwarz' primitive (*P*) surface, Schwarz' diamond (*D*) surface and Schoen's gyroid (*G*) surface (Schoen, 1970) are the most symmetric in both \mathbb{E}^3 and \mathbb{H}^2 (Fig. 1). The two-dimensional asymmetric patch of the *P*, *D* and *G* surfaces is a hyperbolic triangle, bounded by mirror lines (Molnar, 2002; Hyde, Ramsden *et al.*, 2003). This patch tiles both \mathbb{H}^2 , as shown in Fig. 1(a), and the three simplest TPMSs, illustrated in Figs. 1(b), 1(c), 1(d). The symmetry group of the tiling is $\star 246$.

¹ This conformal (*i.e.* angle-preserving) model maps \mathbb{H}^2 onto the interior of a unit circle, with ever-increasing length shrinkage from the centre to the boundary, so that the boundary of the circle in fact represents points at infinity in \mathbb{H}^2 (Hilbert & Cohn-Vossen, 1952). A hyperbolic geodesic – the analogue of a Euclidean straight line – is represented in the disc by a circular arc that meets the boundary circle at right angles. Parallel geodesics in \mathbb{H}^2 are presented by circular arcs that just meet at the disc boundary; hyperparallel geodesics map to circular arcs that have no points in common.

An online enumeration of conventional tilings commensurate with the *P*, *D* and *G* surfaces and their corresponding TPMS reticulations is located at Hyde *et al.* (2010), and details of the process are given in Hyde *et al.* (2006). A complete description of kaleidoscopic tilings, whose asymmetric domains and orbifolds are bounded by mirror lines, is given in Ramsden *et al.* (2009). That study considered only tilings of \mathbb{H}^2 that are composed entirely of tiles topologically equivalent to a compact disc, a constraint that is consistent with the usual implementation of Delaney–Dress tiling theory. The resulting patterns in \mathbb{E}^3 are embedded single-component, 3-periodic nets.

This restriction is convenient and mathematically useful, though limiting, since Euclidean and hyperbolic spaces can be tiled by a broader class of tiles also. In this paper and its partner publication, we explore patterns that emerge from hyperbolic tilings whose tiles are infinite, rather than compact, and we term these tilings *free tilings*. These examples significantly broaden the catalogue of resulting patterns in \mathbb{E}^3 , since multiple interwoven patterns are generally (though not always) formed with more than one disjoint component.

In this paper we explore free tilings whose hyperbolic tiles are infinite ribbon-like strips with boundaries composed of finite edge segments that meet at vertices of degree 3 or more. Switching focus from the tiles to the edges, we see that these edges form 'forests' (*i.e.* collections of trees). These have been explored to a limited extent previously (Hyde & Ramsden, 1999; Hyde & Oguey, 2000; Hyde & Ramsden, 2000b,c; Hyde, Larsson *et al.*, 2003; Hyde, Ramsden *et al.*, 2003; Hyde &

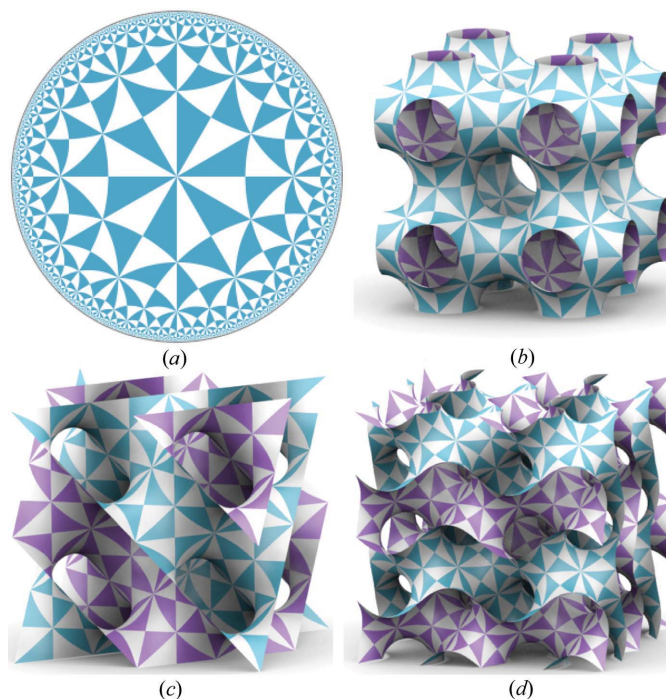


Figure 1
(a) $\star 246$ tiling on the Poincaré disc model of \mathbb{H}^2 . The cubic genus-3 TPMSs. (b) *P* surface, (c) *D* surface and (d) *G* surface. All are covered by the same triangular tiling, and an orientation preserving subgroup of $\star 246$. The blue and purple colours show the two distinct channels of the surfaces.

Ramsden, 2003). After projection onto a TPMS, these forests become periodic arrays of multi-component nets with varying degrees of entanglement.

To date, *ab initio* enumeration of multiple nets has been elusive. Here we describe in some detail the simplest examples of multiple nets. The analysis draws on earlier work (Hyde & Oguey, 2000), now extended. The paper deals in detail with the simplest cases, namely multiple regular degree-3 nets, generated from regular ribbon tilings using an extension of Delaney–Dress tiling theory. First, we sketch a route to enumeration of free tilings. Second, we extend tilings beyond the kaleidoscopic cases due to Coxeter orbifolds, to include examples of stellate orbifolds of \mathbb{H}^2 , where the symmetry of the tiling is composed solely of rotations. These examples admit a two-parameter family of embeddings of the tilings in \mathbb{H}^2 and the TPMSs, analogous to embedding parallelograms in the two-dimensional Euclidean plane. Those tools are then used to construct a catalogue of degree-3 regular ribbon tilings on the *P*, *D* and *G* surfaces, and their associated embeddings in \mathbb{E}^3 as multiple nets. We also describe some examples of multiple degree-4 and degree-6 nets from regular ribbon tilings, providing a template for exhaustive enumeration of other cases.

A characteristic of the Euclidean patterns that result from these tilings is their various entangled forms. We discuss various measures of entanglement and introduce a numerical tightening algorithm, suitable for tangled nets, that offers a partial resolution of the vexed issue of distinguishing various entanglements of multiple nets.

2. Accommodating free tilings within Delaney–Dress tiling theory

Combinatorial tiling theory allows exhaustive enumeration of symmetric tilings of (in principle) any simply connected space by finite, simply connected tiles. It has been developed in detail for \mathbb{H}^2 , \mathbb{E}^2 , S^2 and \mathbb{E}^3 (Huson, 1993; Delgado-Friedrichs & Huson, 1999; Delgado-Friedrichs, 2001). Its constructive key is a finite Delaney–Dress tiling symbol (or ‘D-symbol’), that provides a canonical and finite encoding of the topology and symmetry of the tiling (Dress, 1987). The D-symbol for a tiling is formed by triangulating tiles of the periodic tiling into *chambers*, where the three vertices of the chamber lie at a vertex, edge and face of the tiling. Symmetrically distinct

chambers are assigned a distinct label and the D-symbol encodes the combinatorics of involutions between chambers. The number of symmetrically distinct faces, edges and vertices of the tiling defines its ‘transitivity’; thus the most symmetric (‘regular’) tilings are vertex-, edge- and face-1-transitive. A unique ordering of complexity may be obtained from a D-symbol, allowing exhaustive enumeration of tilings by their complexity (Delgado-Friedrichs, 2003). A fuller application of this approach to tilings of \mathbb{H}^2 and TPMSs can be found in Ramsden *et al.* (2009).

The combinatorial approach can be used to characterize (or conversely to construct) an example of a regular tiling of \mathbb{H}^2 with symmetry group $\star 2223$. The tiling contains vertices at $\star 3$ sites (the site where three mirrors intersect) and edges along both mirror edges of the $\star 2223$ orbifold linking $\star 3$ and $\star 2$ sites, forming a tessellation of \mathbb{H}^2 of degree-6 by quadrangles (a $\{4, 6\}$ regular tiling, Fig. 2). We fragment a single tile into constituent chambers and label chamber vertices 0, 1, 2 according to their location on tiling vertices, edges and faces, respectively. Edges are labelled by the label of the opposite vertex. Two distinct chambers, *A* and *B*, result. The D-symbol is built as follows. First, the symmetry of the tiling is encoded by determining the effect of involutions in all three edges of each chamber. Involutions are denoted s_0, s_1, s_2 , where the subscript determines the edge through which the chamber is mapped. For example, chamber *A* is mapped to chamber *B* through the chamber edge connecting the $\star 3$ site (a ‘0’ vertex) and the opposite $\star 2$ site that lies within a face (and is therefore a ‘2’ vertex). The s_1 involution therefore maps *A* to *B*. The complete combinatorics make up the symmetric encoding of the tiling’s D-symbol. Its topology ($\{4, 6\}$) is encoded by integer entries for the order of the cyclic *AB* permutation around vertices and faces (m_{12} and m_{01} , respectively). The resulting D-symbol is tabulated in Fig. 2, where the symmetry group of the tiling is $\star 2223$.

The key to generating free tilings with infinite tiles is the recognition that free tilings transform to conventional tilings (containing finite tiles) by the addition of a finite number of symmetrically distinct edges. We therefore extend the conventional combinatorial approach to infinite tiles by deleting edges from a conventional tiling while preserving the original Delaney–Dress triangulation. By associating each free tiling with a conventional tiling, free tilings inherit the enumerable structure of D-symbols. These free tilings are denoted by

the original Delaney–Dress encoding with an additional signifier, namely a $\bar{1}$ -vertex rather than the standard 1-vertex, on the chambers that now contain a ‘ghosted’ edge. The symbol may be tabulated identically to regular tilings; however the chambers containing real edges are given in bold font and the chambers with ghosted edges in regular font. We note that the development of free tiling theory is still in progress. However, for the purposes of this paper, the approach proves useful.

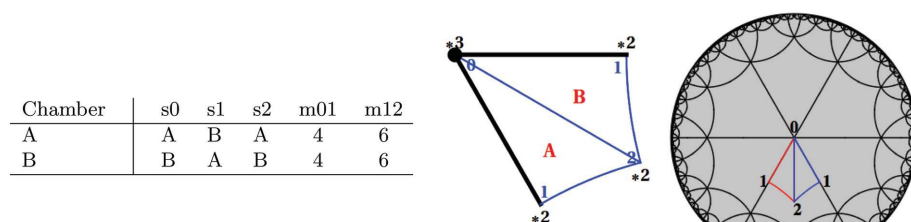


Figure 2

The Delaney–Dress representation of a regular $\{4, 6\}$ tiling on the $\star 2223$ orbifold. The edge passes along the mirror boundary from the $\star 3$ site to the $\star 2$ site. See the text for further details.

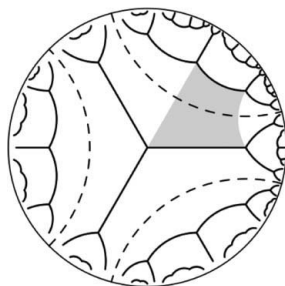


Figure 3
A close-packed array of regular degree-3 trees (full edges) in the hyperbolic plane, separated by geodesic lines that define the skeleton of the tile (dashed). The shaded polygon represents a portion of an infinite ribbon tile, that extends infinitely along the skeleton.

This encoding is complicated by the fact that most free tilings may be constructed from multiple distinct conventional tilings: if two conventional tilings differ only by a single edge (and have different Delaney–Dress encodings), and this particular edge is ghosted, the same free tiling will result and will be classified by two distinct encodings. The unique encoding of a free tiling is chosen to be the simplest among all possible encodings, as defined by the number of chambers within the triangulation of a single orbifold domain. Where there exist multiple simplest encodings of a single free tiling, the unique encoding is chosen to be that which has the least complexity according to the D-symbol ordering (Delgado-Friedrichs, 2003).

The free tilings considered in this paper are regular ribbon tilings of \mathbb{H}^2 . Recall that regular tilings are vertex-, edge- and face-1-transitive. A Euclidean ribbon is a strip whose ‘skeleton’ – the central axis that is maximally distant from the ribbon edges – is an unbranched line. Similarly, a hyperbolic ribbon is characterized by an unbranched line-shaped skeleton. Unlike Euclidean ribbons however, hyperbolic ribbons are bounded by finite edges and contain an infinite number of vertices. The edges and vertices belong to hyperbolic trees (Hyde & Oguey, 2000). The edges of degree-3 ribbon tilings form degree-3 trees. Like their Euclidean cousins, regular hyperbolic ribbon tiles exhibit translational symmetry, by translations along the ribbon’s skeleton. The most symmetric ribbon tilings are of special importance among the hierarchy of free tilings, since their edges form close-packed trees in \mathbb{H}^2 , whose vertex density in the hyperbolic plane is maximal (Hyde & Oguey, 2000). We call these close-packed examples ‘dense’ tilings. While this notion of close packing does not carry over to the resulting Euclidean

Chamber Class	s0	s1	s2	m01	m12
A	A	B	A	4	6
B	B	A	B	4	6

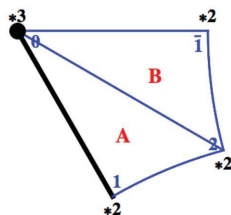


Figure 4
The Delaney–Dress representation of a regular ribbon tiling on the $*2223$ orbifold: $124RT$. The edge passes along the mirror boundary from the $*3$ site to the $*2$ site.

Chamber Class	s0	s1	s2	m01	m12
A	A	B	A	3	9
B	C	A	C	3	9
C	B	C	B	3	9

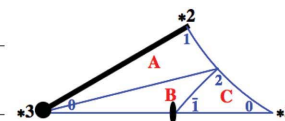


Figure 5
The regular ribbon tiling of the $*2*23$ orbifold. The decoration passes from the $*3$ site, along the mirror boundary, to the $*2$ site. This tiling is referred to by the label $129RT$.

embeddings of ribbon tilings, the resulting patterns are nevertheless densely arrayed on the TPMS.

A simple example of a dense, regular degree-3 ribbon tiling is shown in Fig. 3. The infinite tile is bounded on both sides by edges of a regular tree and its skeleton is a hyperbolic geodesic.

Possible symmetries of regular degree-3 dense ribbon tilings can be readily deduced from their 1-transitivity. Edge transitivity implies that the degree-3 vertex of the tile boundary must have threefold rotational symmetry, so its site symmetry is either 3 (a threefold rotation centre) or $*3$. Further, since all vertices are equivalent, edge midpoints must have site symmetry 2 or $*2$. Their translational symmetry within individual ribbons may be due to some combination of $*2$ symmetries, twofold rotations, ‘o’ or ‘x’. Among the admissible groups that are commensurate with the cubic TPMSs (Robins *et al.*, 2004a), four fit these criteria: $*2223$ (group 124), $2*23$ (group 129), 2223 (group 118) and $23\times$ (group 121). Regular ribbon tilings from the $23\times$ orbifold display additional symmetry, so that these examples adopt a symmetry group of $2*23$ (a supergroup of $23\times$). We therefore analyse regular ribbon tilings with symmetry groups $*2223$, $2*23$ and 2223 , belonging to the Coxeter, hat and stellate orbifold classes, respectively.

The Coxeter class allows a single, regular degree-3 ribbon tiling. The tile edge runs from the $*3$ sites along the mirror boundary to a $*2$ site. The decoration has boundary vertices at the $*3$ site, edge midpoints at the $*2$ site and an infinite translation generated by the parallel mirrors of the remaining two $*2$ sites. This decoration is shown in Fig. 4 along with a table representing its Delaney–Dress encoding. We name this tiling for convenience ‘ $124RT$ ’: R for ‘regular’, T for the ‘tree-like’ topology of the tile boundaries and symmetry of group 124.

The single degree-3 regular ribbon tiling ($129RT$) from the hat class ($2*23$) contains an edge passing from the $*3$ site along the mirror boundary to the $*2$ site (Fig. 5).

Lastly, a stellate regular ribbon tiling is possible (2223). The orbifold is decorated by an edge passing from the centre of threefold rotation to a centre of twofold rotation. Fig. 6 shows the regular ribbon tiling tabular representation along with an image of the decorated orbifold. This tiling is referred to as $118RT$.

3. Embedding abstract tilings in two dimensions

The D-symbol is an encoding of the topology and symmetry of a tiling. It encodes a decoration of an orbifold and distinct

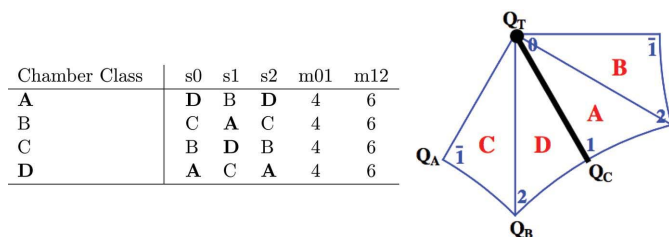


Figure 6
Representation of the regular ribbon tiling on the 2223 orbifold, 118RT. The twofold sites are labelled Q_A , Q_B and Q_C , the threefold site is at Q_T . The edge is from Q_T to Q_C .

embeddings of the tiling can be constructed that share the same orbifold. Fig. 1, for example, shows four different surfaces that share the $\star 246$ orbifold. To generate an embedded tiling, the set of generators for the group corresponding to the orbifold must be specified within the embedding space.

The two-dimensional asymmetric patch (or fundamental domain) of the P , D and G surfaces is a triangle bounded by in-surface mirror (curvilinear) lines meeting at angles of $\pi/2$, $\pi/4$ and $\pi/6$ at the corners of the patch – a $\star 246$ triangle. That follows from the differential geometry of these TPMSs, but it is not readily apparent from a Euclidean perspective. In fact, those two-dimensional mirrors can coincide with mirror planes, twofold axes of rotational symmetry, or no Euclidean isometries at all in \mathbb{E}^3 , depending on the TPMS (Ramsden *et al.*, 2009).

The asymmetric patch of any $\star 246$ tiling corresponds to a single $\star 246$ triangle bounded by (hyperbolic) lines with equal vertex angles to those on the cubic TPMSs. In contrast to the three-dimensional examples, this triangle is unique in \mathbb{H}^2 . Its three edges define mirror lines in \mathbb{H}^2 induced by the symmetries of $\star 246$: R_1 , R_2 and R_3 . The reflection R_1 maps across the line passing from the $\star 6$ site through the $\star 2$ site, R_2 from the $\star 2$ site through the $\star 4$ site and R_3 from the $\star 6$ site through the $\star 4$ site (Robins *et al.*, 2004a; Molnar, 2002). The infinite $\star 246$ pattern is shown in Fig. 1(a).

In order to form tilings on the cubic TPMSs, we require embeddings of $\star 2223$, $2\star 23$ and 2223 orbifolds as subgroups of $\star 246$. That constrains the orbifold geometries to be commensurate with the parent $\star 246$ geometry so that symmetry sites of the orbifold must coincide with symmetry elements of the $\star 246$ group.

3.1. Embedding $\star 2223$

The regular degree-3 Coxeter ribbon tiling, with symmetry group $\star 2223$, has a unique embedding in the $\star 246$ tiling pattern (Robins *et al.*, 2004a). (Here we refer to the tiling formed by $\star 246$ triangles as the ‘ $\star 246$ tiling’.) This embedded orbifold is composed of exactly two $\star 246$ triangles, glued along R_3 (the mirror passing from the $\star 6$ site to the $\star 4$ site). This amalgamated domain has two $\star 2$ sites from the original two triangles, an additional $\star 2$ site from a gluing of two $\star 4$ sites and a $\star 3$ site from a gluing of two $\star 6$ sites. One fundamental domain of the $\star 2223$ orbifold embedded in the $\star 246$ is shown

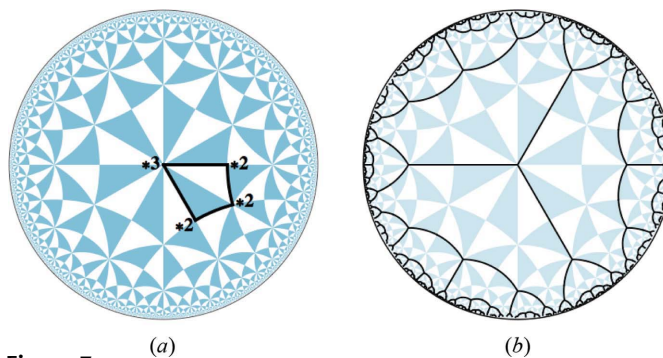


Figure 7
(a) The embedding of the $\star 2223$ orbifold in the $\star 246$ tiling of \mathbb{H}^2 : two $\star 246$ triangles fused along an R_3 boundary. (b) $\star 246_{124RT}(\cosh^{-1}(3))$, the embedded regular ribbon tiling of $\star 2223$.

in Fig. 7(a). The $\star 2223$ orbifold has an abstract symmetry (automorphism) along the axis passing from the $\star 3$ site to the opposite $\star 2$ site. Once the orbifold is embedded, however, this abstract symmetry aligns with the R_3 reflection of the $\star 246$ tiling: the automorphism of the orbifold corresponds to a conjugacy of the $\star 246$ map, so we need only consider one form (Ramsden *et al.*, 2009). The embedded regular ribbon tiling from Fig. 4, denoted $\star 246_{124RT}(\cosh^{-1}(3))$, is shown in Fig. 7(b), where $\cosh^{-1}(3)$ denotes the edge length of the trees in \mathbb{H}^2 . We label the cases as $\star 246_{NRT}(l)$, where N denotes the group number (*cf.* Robins *et al.*, 2004a) and l is the edge length.

3.2. Embedding $2\star 23$

The hat orbifold, $2\star 23$, also has an embedding, which can be demonstrated as follows. Consider the orbifold formed by gluing a pair of $2\star 23$ orbifolds around the twofold rotation site. This forms a $\star 2323$ (Coxeter) orbifold, which uniquely embeds (Fig. 8a). As in the previous Coxeter case, the automorphism of the $2\star 23$ orbifold (an abstract mirror symmetry on the axes passing from the $\star 3$ site to the twofold rotation) is a conjugacy of the $\star 246$ tiling, so we need only consider a single automorphic embedding of the orbifold. Fig. 8(b) shows the embedding of the regular ribbon tiling with symmetry group $2\star 23$, $\star 246_{129RT}(\cosh^{-1}(5))$.

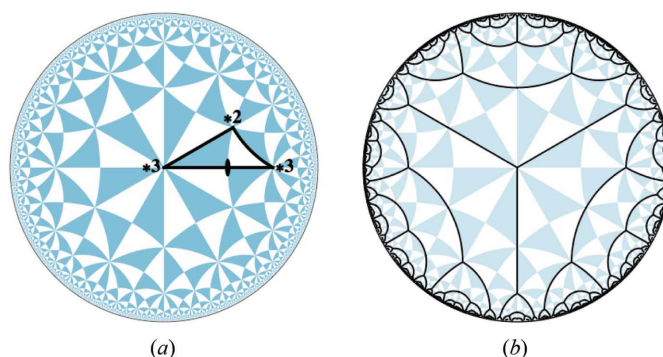


Figure 8
(a) The unique embedding of the $2\star 23$ orbifold into the $\star 246$ tiling of \mathbb{H}^2 . (b) $\star 246_{129RT}(\cosh^{-1}(5))$, the embedded regular ribbon tiling with symmetry group $2\star 23$ (Fig. 5).

3.3. Embedding 2223

In contrast to the Coxeter and hat cases, stellate orbifolds, which contain rotation centres, have an unlimited number of embeddings within $\star 246$. In short, the stellate case leads to a two-parameter family of orbifold domains. Possible locations of the rotation centres of a single orbifold domain are confined to a Euclidean subset of discrete locations in \mathbb{H}^2 , indexed by the two integer indices in $\mathbb{Z} \times \mathbb{Z}$. As a result of this ordered Euclidean subdomain of \mathbb{H}^2 , we may index all possible quadrilateral domains of the 2223 orbifold exactly by the indices of vertices of parallelograms of unit area. (Full details of this derivation are given in Appendix A. Fig. 37 shows the $\mathbb{Z} \times \mathbb{Z}$ grid within a $\pi/3$ sector of the discretization of \mathbb{H}^2 by 2223.)

Each distinct embedding of a 2223 stellate orbifold into the $\star 246$ tiling of \mathbb{H}^2 leads to a distinct embedded free tiling of \mathbb{H}^2 , following the prescription for tile edges given in Fig. 6. Recall that the 2223 regular free tiling is formed by decorating the orbifold by a single edge (Fig. 6). For convenience, we need only specify the generator defining the midpoint of this edge (*i.e.* the coprime pair located at Q'_C , *cf.* Appendix A) to determine our embedded pattern. We list the free tilings by twice the length of this asymmetric unit (since the edge unit

shown in Fig. 6 is half of the distance between $\star 3$ sites, the full edge length), as the reference frame definitions are not unique, but the length of the edge will remain fixed in all incarnations. We therefore enumerate all coprime integer pairs and calculate resulting edge lengths from standard hyperbolic geometry to specify all examples of regular degree-3 free tilings. This also allows us to order all examples in a one-parameter family, by increasing edge length. Hyperbolic trigonometry gives exact integer solutions for most lower-order cases. This is not possible for one example, edge length $\cosh^{-1}(675)$, which is approximated from a numerical computation of the edge length as $\cosh^{-1}(675.002)$.

The shortest-edge members of this stellate family in fact lift to higher symmetries, owing to their regular shape. The simplest example, formed when Q'_C (the edge midpoint) is located at the $\{0, 1\}$ site, or equivalently $\{1, 0\}$ (Fig. 37), has symmetry group $\star 2223$. The next member, with Q'_C located at $\{1, 1\}$, also has extra symmetry ($2\star 23$). All subsequent members have symmetry group 2223. Exhaustive enumeration of all stellate examples therefore also yields the Coxeter and hat cases discussed above.

The first exact members of the family of degree-3, regular, dense free tilings commensurate with $\star 246$ are tabulated and

edge length	coprime pairs	tiling name
$\cosh^{-1}(3)$	$\{0, 1\}, \{1, 0\}$	$\star 246_{124RT}(\cosh^{-1}(3))$
$\cosh^{-1}(5)$	$\{1, 1\}$	$\star 246_{129RT}(\cosh^{-1}(5))$
$\cosh^{-1}(15)$	$\{1, 2\}, \{2, 1\}$	$\star 246_{118RT}(\cosh^{-1}(15))$
$\cosh^{-1}(53)$	$\{1, 3\}, \{3, 1\}$	$\star 246_{118RT}(\cosh^{-1}(53))$
$\cosh^{-1}(99)$	$\{2, 3\}, \{3, 2\}$	$\star 246_{118RT}(\cosh^{-1}(99))$
$\cosh^{-1}(195)$	$\{1, 4\}, \{4, 1\}$	$\star 246_{118RT}(\cosh^{-1}(195))$
$\cosh^{-1}(675)$	$\{3, 4\}, \{4, 3\}$	$\star 246_{118RT}(\cosh^{-1}(675))$
$\cosh^{-1}(725)$	$\{1, 5\}, \{5, 1\}$	$\star 246_{118RT}(\cosh^{-1}(725))$

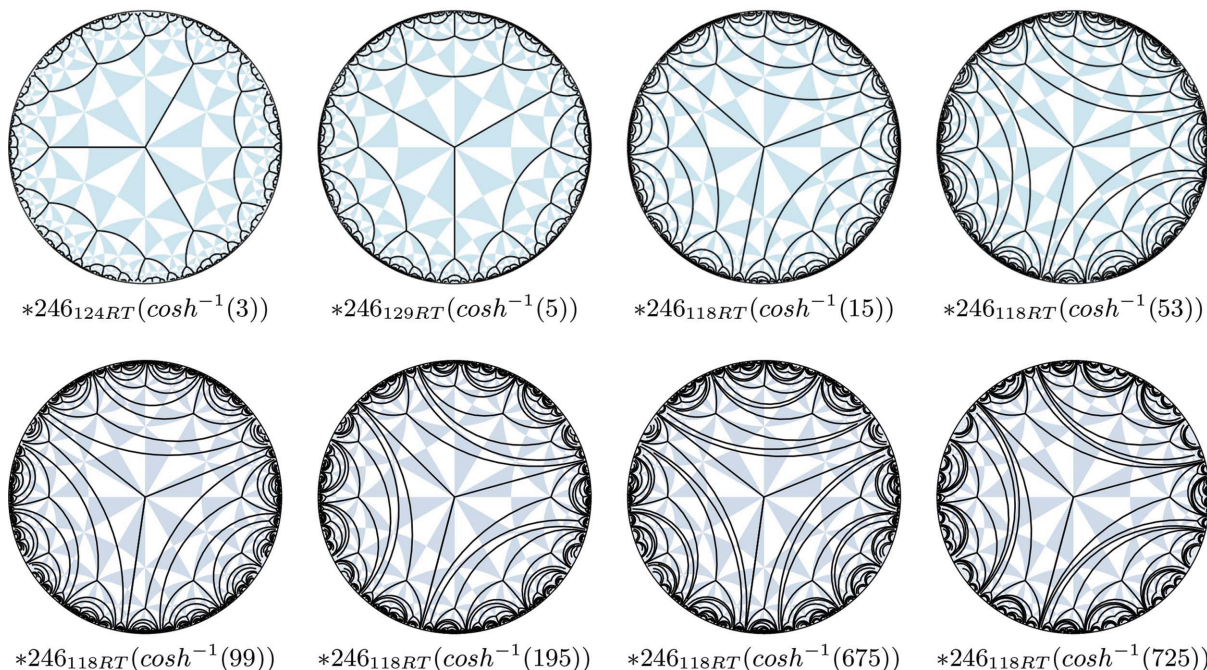


Figure 9 Images of the eight simplest embedded degree-3 regular ribbon tilings, with names given below the images.

illustrated in Fig. 9. The family converges to a simple tiling with edges of infinite length, containing a single degree-3 vertex.

4. Degree-3 interpenetrating networks

Just as planar 2-periodic patterns in the Euclidean plane can be ‘rolled up’ to form 1-periodic patterns on the surface of a cylinder, these regular (6-periodic) free tilings of \mathbb{H}^2 can be projected onto the surfaces of the P , D and gyroid *via* a covering map, to give 3-periodic free tilings of these TPMSs. This process is described in detail in Ramsden *et al.* (2009) and Evans (2011). The edges and vertices of these tilings define TPMS *reticulations*. The reticulation is embedded both on the TPMS and in \mathbb{E}^3 ; the latter embedding defines a pattern of nets in \mathbb{E}^3 . To construct these reticulations, we map the decorated asymmetric domain (corresponding to a single orbifold) of \mathbb{H}^2 (*via* the related domain of \mathbb{S}^2) to an asymmetric (orbifold) domain of the TPMS, using the integral Weierstrass–Enneper equations that define the surface embedding in \mathbb{E}^3 (Fogden & Hyde, 1992).

The isometries of the surface orbifold build the infinite surface; these (hyperbolic) isometries correspond – in most cases – to three-dimensional Euclidean isometries, so that an orbifold on a surface is equivalent to a three-dimensional space group. This correspondence is weakened on the gyroid, since – in contrast to the P and D surfaces – the hyperbolic reflections ($\star 2$ and $\star 3$ isometries *etc.*) are not realized on this surface as Euclidean isometries. Therefore all Coxeter and hat tilings on the G (such as the $\star 2223$ and $2\star 23$ free tilings) embed with Euclidean symmetries given by the related stellate orbifold, formed by retaining only the rotation centres (2223). The correspondence between the \mathbb{H}^2 orbifold symmetry and the related space groups for the simpler TPMSs will be published in detail elsewhere (Hyde *et al.*, 2013). A summary of the space groups corresponding to the orbifolds used in this paper is given in Appendix B.

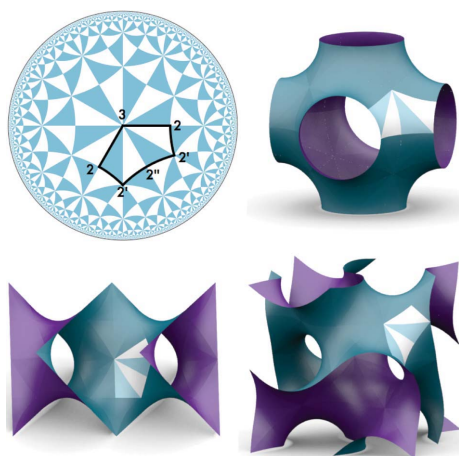


Figure 10

The vertices and edges of a free tiling contained within one fundamental domain in \mathbb{H}^2 are transferred to the corresponding patch on each TPMS. The correspondence between a patch in \mathbb{H}^2 and a patch on each of the surfaces is shown for the stellate symmetry group 2223 .

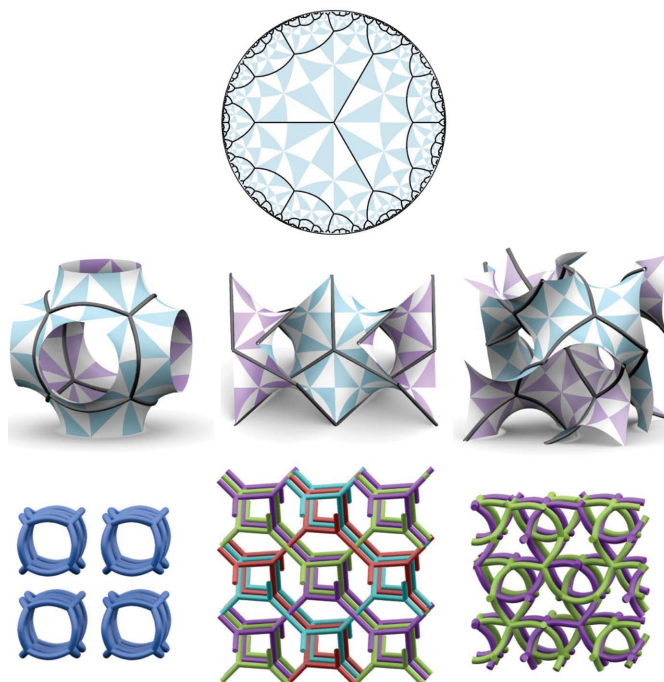


Figure 11

(Top) The Coxeter ($\star 2223$) $\star 246_{124RT}(\cosh^{-1}(3))$ regular, dense degree-3 ribbon tiling of \mathbb{H}^2 . (Middle) The projection of this tiling to (from left to right) the P , D and G (gyroid) surfaces. (Bottom) Resulting network structures in \mathbb{E}^3 : from left to right $P_{124RT}(\cosh^{-1}(3))$, $D_{124RT}(\cosh^{-1}(3))$ and $G_{124RT}(\cosh^{-1}(3))$. Details of these structures are found in Tables 1, 2 and 3.

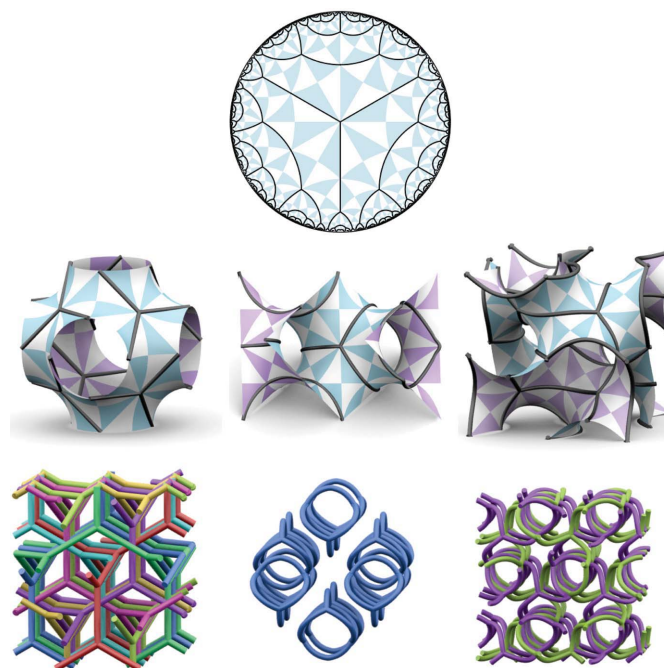


Figure 12

(Top) The hat ($2\star 23$) $\star 246_{129RT}(\cosh^{-1}(5))$ regular, dense degree-3 ribbon tiling of \mathbb{H}^2 . (Middle) The projection of this tiling to (from left to right) the P , D and G surfaces. (Bottom) Resulting network structures in \mathbb{E}^3 : from left to right $P_{129RT}(\cosh^{-1}(5))$, $D_{129RT}(\cosh^{-1}(5))$ and $G_{129RT}(\cosh^{-1}(5))$. Details of these structures are found in Tables 1, 2 and 3.

Table 1

Multiple nets that result from dense ribbon tilings on the P surface.

'# comp.' is the number of connected components, $n*$ designates infinitely many 2-periodic layers with n orientations. The net topologies are labelled as follows: θ is the theta graph; **tet**, **cub** denote the polyhedral graphs of tetrahedron and cube edges; **hcb** is the 2-periodic hexagonal net; **srs** is the 3-periodic regular degree-3 net (names adopted from O'Keeffe *et al.*, 2008). Listings of link types and counts (e.g. 92 Hopf links) are generated by analysis using the *TOPOS* package (Blatov, 2006), m - m -rings refers to the pairwise interaction of rings of length m .

Structure	Figure	# comp.	Topology	Notes
$P_{124RT}(\cosh^{-1}(3))$	Fig. 11	∞	cub	No catenation between disjoint nets
$P_{129RT}(\cosh^{-1}(5))$	Fig. 12	8	srs	Chiral (all nets like-handed), class IIIb, 10-10-rings: 92 Hopf links
$P_{118RT}(\cosh^{-1}(15))$	Fig. 13	4*	hcb	(111) orientations, 6-6-rings: 18 Hopf links
$P_{118RT}(\cosh^{-1}(53))$	Fig. 14	8	srs	Chiral, class IIIb, 10-10-rings: 168 Hopf links, 16 higher-order links
$P_{118RT}(\cosh^{-1}(99))$	Fig. 14	64	srs	Chiral, class Ib, 10-10-rings: 832 Hopf links and 25 higher-order links
$P_{118RT}(\cosh^{-1}(195))$	Fig. 14	∞	cub	Hopf links
$P_{118RT}(\cosh^{-1}(675))$	Fig. 14	64	srs	Chiral, class Ib, 10-10-rings: 1442 Hopf links and 181 higher-order links
$P_{118RT}(\cosh^{-1}(725))$	Fig. 14	8	srs	Chiral, class IIIb, 10-10-rings: 118 Hopf links and 93 higher-order links

Table 2

Multiple nets that result from dense ribbon tilings on the D surface.

See Table 1 for details.

Structure	Figure	# comp.	Topology	Notes
$D_{124RT}(\cosh^{-1}(3))$	Fig. 11	4	srs	Chiral, class Ib, 10-10-rings: 36 Hopf links
$D_{129RT}(\cosh^{-1}(5))$	Fig. 12	∞	tet	No catenation between disjoint nets
$D_{118RT}(\cosh^{-1}(15))$	Fig. 13	4*	hcb	(111) orientations, 6-6-rings: 12 Hopf links
$D_{118RT}(\cosh^{-1}(53))$	Fig. 15	32	srs	Chiral, class IIIb, 10-10-rings: 426 Hopf links, 16 higher-order links
$D_{118RT}(\cosh^{-1}(99))$	Fig. 15	4	srs	Chiral, class Ib, 10-10-rings: 90 Hopf links, 24 higher-order links
$D_{118RT}(\cosh^{-1}(195))$	Fig. 15	4	srs	Chiral, class Ib, 10-10-rings: 472 Hopf links, 62 higher-order links
$D_{118RT}(\cosh^{-1}(675))$	Fig. 15	4	srs	Chiral, class Ib, 10-10-rings: 84 Hopf links, 30 higher-order links
$D_{118RT}(\cosh^{-1}(725))$	Fig. 15	4	srs	Chiral, class IIIb, 10-10-rings: 896 Hopf links, 242 higher-order links

Table 3

Multiple nets that result from dense ribbon tilings on the G surface.

See Table 1 for details.

Structure	Figure	# comp.	Topology	Notes
$G_{124RT}(\cosh^{-1}(3))$	Fig. 11	2	srs	Chiral, class Ia, 10-10-rings: 18 Hopf links, 1 higher-order link
$G_{129RT}(\cosh^{-1}(5))$	Fig. 12	2	srs	Chiral, class IIa, 10-10-rings: 23 Hopf links, 3 higher-order links
$G_{118RT}^+(\cosh^{-1}(15))$	Fig. 13	4*	hcb	(111) orientations, 6-6-rings: 30 Hopf links
$G_{118RT}^-(\cosh^{-1}(15))$	Fig. 13	∞	θ	No catenation between disjoint nets
$G_{118RT}^+(\cosh^{-1}(53))$	Fig. 16	54	srs	Chiral, class IIIb ($3 \times 3 \times 3$) $\times 2$, 10-10-rings: 725 Hopf links, 19 higher-order links
$G_{118RT}^-(\cosh^{-1}(53))$	Fig. 16	2	srs	Chiral, class IIa, 10-10-rings: 25 Hopf links, 17 higher-order links
$G_{118RT}^+(\cosh^{-1}(99))$	Fig. 16	54	srs	Chiral, class Ib ($6 \times 3 \times 3$), 10-10-rings: 728 Hopf links, 25 higher-order links
$G_{118RT}^-(\cosh^{-1}(99))$	Fig. 16	2	srs	Chiral, class Ia, 10-10-rings: 30 Hopf links, 17 higher-order links
$G_{118RT}^+(\cosh^{-1}(195))$	Fig. 16	2	srs	Chiral, class Ia, 10-10-rings: 598 Hopf links, 61 higher-order links
$G_{118RT}^-(\cosh^{-1}(195))$	Fig. 16	2	srs	Chiral, class Ia, 10-10-rings: 102 Hopf links, 23 higher-order links
$G_{118RT}^+(\cosh^{-1}(675))$	Fig. 16	54	srs	Chiral, class Ib ($6 \times 3 \times 3$), 10-10-rings: 1092 Hopf links, 140 higher-order links
$G_{118RT}^-(\cosh^{-1}(675))$	Fig. 16	2	srs	Chiral, class Ia, 10-10-rings: 116 Hopf links, 37 higher-order links
$G_{118RT}^+(\cosh^{-1}(725))$	Fig. 16	54	srs	Chiral, class IIIb ($3 \times 3 \times 3$) $\times 2$, 10-10-rings: 1139 Hopf links, 246 higher-order links
$G_{118RT}^-(\cosh^{-1}(725))$	Fig. 16	2	srs	Chiral, class IIa, 10-10-rings: 168 Hopf links, 56 higher-order links

The correspondence between a single copy of the 2223 orbifold in \mathbb{H}^2 and the related patch on each of the TPMSs is shown in Fig. 10. The other symmetry groups can be inferred from this, e.g. $\star 2223$ occupies half of a 2223 domain.

The covering map for the gyroid is a special case, owing to the fact that the surface contains no (Euclidean) reflection symmetries corresponding to the hyperbolic reflections of the $\star 246$ group. For this surface, there are two distinct covering maps of the surface for tilings in \mathbb{H}^2 that are commensurate

with $\star 246$ (Robins *et al.*, 2005). Tilings in \mathbb{H}^2 that are achiral (unchanged under any of the $\star 246$ reflections, apart from possible rotations or translations) will render two identical structures on the surface and hence in \mathbb{E}^3 , and tilings that do not have this inherent symmetry will have two distinct embeddings. Since the Coxeter and hat tilings are achiral, just one Euclidean pattern is generated for each tiling on the gyroid; however, all the stellate hyperbolic tilings give a pair of patterns in \mathbb{E}^3 . These two covering maps can be distinguished

in Fig. 10 by placing the hyperbolic pattern on the outward-facing (green) or the inward-facing (purple) of the highlighted surface domain, respectively.

In general, the infinite collection of disjoint degree-3 trees in \mathbb{H}^2 (the hyperbolic forest) projects to a collection of interpenetrating nets in \mathbb{E}^3 . Since all the trees in the forest are symmetrically identical, and the placement of each tree is identical in the TPMS, the patterns in \mathbb{E}^3 must be made up of identical disjoint component nets. What are these possible nets? Regular, free degree-3 ribbon tilings with symmetry groups $\star 2223$, $2\star 23$ and 2223 have vertices at all $\star 6$ sites. Those sites are the singular ‘flat points’ of the minimal surfaces; Hopf’s index theorem implies that there are eight of these per primitive unit cell of the oriented TPMS (Hyde, 1989; Fischer & Koch, 1987). Since the tilings are regular (1-transitive), they have symmetrically identical edges and vertices both in \mathbb{H}^2 and on the TPMS. The curvilinear ‘e-nets’ (Ramsden *et al.*, 2009) induced by the surface reticulations are therefore regular. Straightening edges to form a barycentric embedding can never increase the transitivity, since this process symmetrizes the net embedding in \mathbb{E}^3 as far as possible (Delgado-Friedrichs & O’Keeffe, 2003). The nets in \mathbb{E}^3 are therefore also regular. Regular degree-3 nets in \mathbb{E}^3 are the 3-periodic **srs** net (Delgado Friedrichs *et al.*, 2003), the 2-periodic **hcb** ($\{6, 3\}$) net (O’Keeffe *et al.*, 2008), a 1-periodic chain multi-graph, with three edges between successive vertices and the 0-periodic (finite) graphs of tetrahedron (**tet**), cube (**cub**) and dodecahedron edges. The dodecahedron edge graph cannot result from these regular forests, since a maximum of eight vertices per unit cell are allowed. One further finite graph is possible, the theta graph (θ), with just two degree-3 vertices. (Though the non-simple theta graph is technically not a net, for convenience here we label it as such.)

The regular degree-3 ribbon tilings therefore afford a systematic technique to enumerate the simplest entanglements of θ , **tet**, **cub**, **hcb** and **srs** nets. The resulting patterns are described in the following section.

4.1. Structure of the Euclidean degree-3 nets

Recall that these regular free tilings necessarily form Euclidean intergrowths of identical nets. So these patterns are characterized topologically by the component net type and number of disjoint components. This information is obtained using either *GAVROG* (Delgado-Friedrichs, 2012) or *TOPOS* (Blatov, 2006) software that affords identification of net

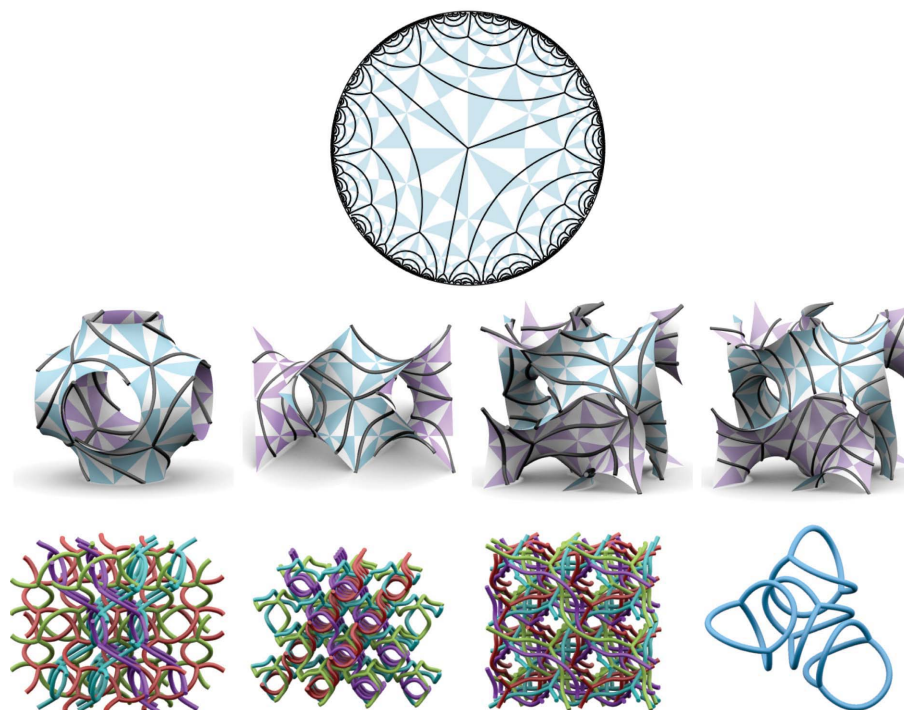


Figure 13

(Top) The shortest-edge member of the stellate (2223) $\star 246_{118RT}(\cosh^{-1}(15))$ regular, dense degree-3 ribbon tiling of \mathbb{H}^2 . (Middle) The projection of this tiling to (from left to right) the P , D and G surfaces (both covering maps). (Bottom) Resulting network structures in \mathbb{E}^3 : from left to right $P_{118RT}(\cosh^{-1}(15))$, $D_{118RT}(\cosh^{-1}(15))$, $G_{118RT}^+(\cosh^{-1}(15))$ and $G_{118RT}^-(\cosh^{-1}(15))$. Details of these structures are found in Tables 1, 2 and 3.

topology with reference to a library of structures (excluding the finite graphs, which we identify by eye from three-dimensional representations of the structures). For our entangled structures, edges are permitted to curve as they trace from one vertex to another. An input file for either *GAVROG* or *TOPOS* has vertices connected by straight edges, thus it is necessary for us to introduce additional degree-2 vertices along the curved edges in order to maintain the entanglement. As a consequence, *GAVROG* fails to identify these exact structures as *e.g.* **srs**. However, *TOPOS* can be used to identify net topology, provided essential added degree-2 vertices are not included in the analysis. The supplementary material contains crystallographic data suitable for *TOPOS* input for all structures presented in this paper: we include one set of data with a minimal number of additional degree-2 vertices necessary to maintain the entanglement, and another set with many additional degree-2 vertices to show the complete edge geometry.²

Quantitative analysis of these structures requires descriptors for the entanglement between nets. (And potentially within individual nets, as discussed in §7 below.) Here we provide the measures developed by Blatov, Proserpio *et al.* to characterize intergrown nets identified in atomic and mole-

² Supplementary material for this paper is available from the IUCr electronic archives (Reference: EO5019). Services for accessing these data are described at the back of the journal.

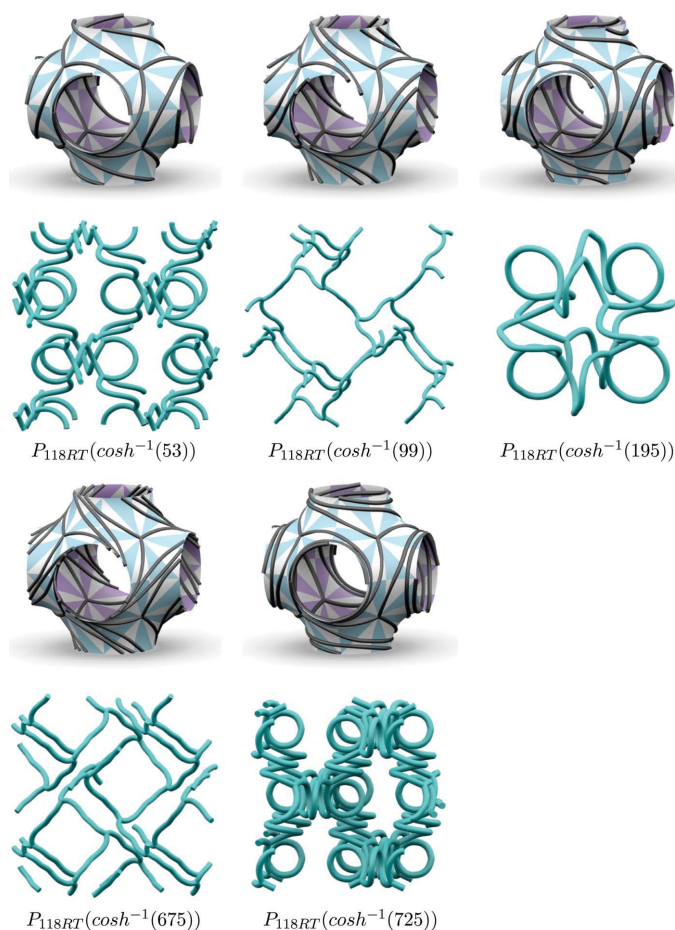


Figure 14
The stellate (2223) $\star 246_{118RT}$ regular, dense degree-3 ribbon tiling family, each on a unit cell of P surface. Below each surface reticulation are views of a single component of the net embeddings in \mathbb{E}^3 . (The names of the structures are shown below each image.) Details of these structures are found in Table 1.

cular crystals (Carlucci *et al.*, 2003; Blatov, 2006) and available as output from *TOPOS* (Blatov, 2006). These are:

- (i) The number of connected components.
- (ii) Symmetry relations between distinct components. For the structures referred to in this paper, the classes can be listed as follows. Class I has only translations: Ia has one translation and Ib has two independent translations. Class II has only rotations: IIa has one distinct rotation and IIb has two distinct rotations. Class III has both translations and rotations: $IIIa$ has a single translation and single rotation, $IIIb$ has multiple translations and a single rotation, $IIIc$ has a single translation and multiple rotations, and $IIId$ has multiple translations and rotations.
- (iii) Entanglement of all cycles of a given size. The entanglements are characterized as either Hopf links (Adams, 2004) or higher-order links, which encompasses all links with a higher crossing number. The number of links considers a single cycle of the structure, and counts the number and types of links passing through this cycle. This measure is a useful guide to distinguishing between distinct entanglements that necessarily have different numbers.

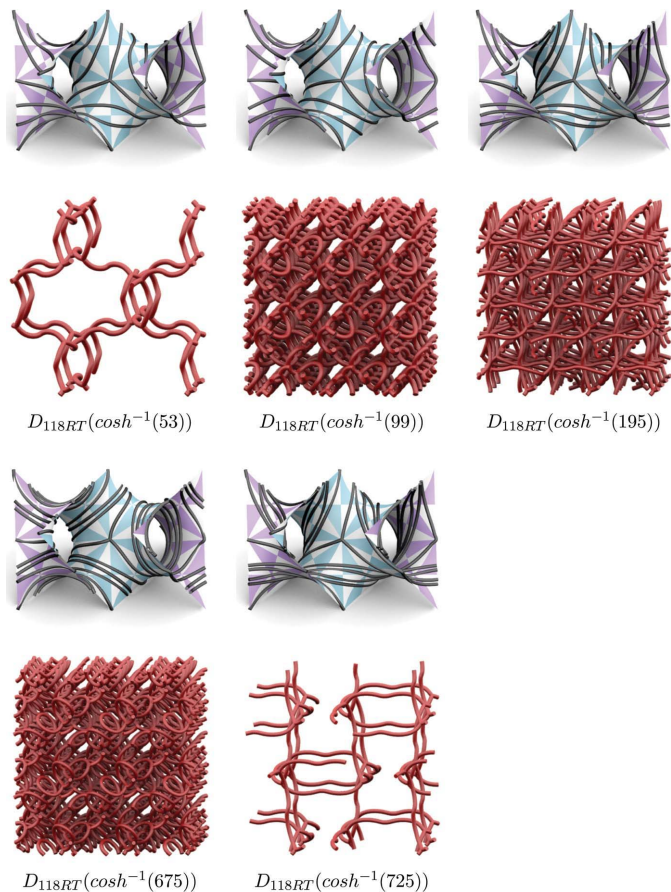


Figure 15
The stellate (2223) $\star 246_{118RT}$ regular, dense ribbon degree-3 tiling family, each on a unit cell of the D surface. Below each surface reticulation are views of a single component of the net embeddings in \mathbb{E}^3 . (The names of the structures are shown below each image.) Details of these structures are found in Table 2.

We summarize the resulting structures in Tables 1, 2 and 3, and provide images for these in Figs. 11–16. The structures are labelled with the tiling name (*cf.* §3) as well as the TPMS. For example, the Euclidean pattern that results from projection of the $\star 246_{118RT}(cosh^{-1}(15))$ tiling to the P surface is labelled $P_{118RT}(cosh^{-1}(15))$. Owing to the pair of distinct Euclidean patterns that arise on the gyroid from chiral hyperbolic tilings (from the stellate cases only, *i.e.* G_{118RT}), a superscript + or – is appended to specify which member of the two possible covering maps of the surface is used (Robins *et al.*, 2005). (Where this is absent, the + and – structures are identical.)

The multiple nets that emerge from this construction are mostly entangled **srs** patterns. Each surface reticulation gives a single example of a (non-threaded) lattice of finite nets, as well as one 2-periodic entangled (**hcb**) example. All other cases within this finite enumeration contain entangled equivalent enantiomers of multiple **srs** nets, from two components to 54. Remarkably, all examples of multiple **srs** nets have distinct entanglement modes according to the link counts of *TOPOS*. The enumeration reveals for example six distinct entanglements of pairs of enantiomeric **srs** nets, all regular ribbon tilings on the gyroid.

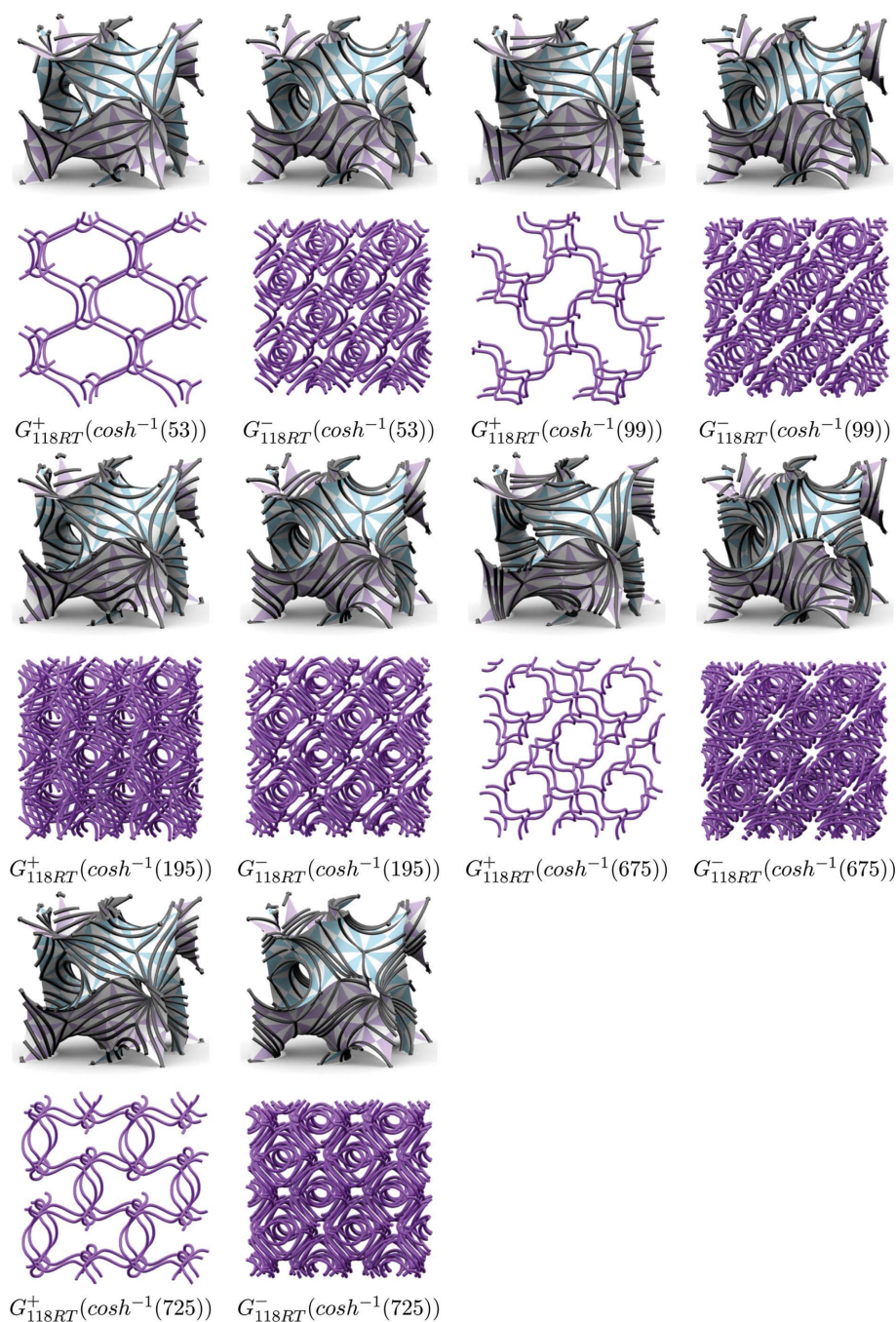


Figure 16
 The stellate (2223) $\star 246_{18RT}$ regular, dense degree-3 ribbon tiling family, each on a unit cell of the G surface. Below each surface reticulation are views of a single component of the net embeddings in \mathbb{E}^3 . (The names of the structures are shown below each image.) Details of these structures are found in Table 3.

It is clear from Tables 1, 2 and 3 that the number of threaded components is not directly correlated with the free tiling edge length. The degree of entanglement can be gauged in part by the link counts listed in Tables 1, 2 and 3: the multiple nets with large numbers of links are more tangled. Those numbers do not increase monotonically for successive members of the stellate family, indicating that entanglement is not simply a function of the edge length of the component trees. That is also clear from Figs. 14, 15 and 16 which show

that the homotopy, or degree of winding (curvature and torsion), of the edges of component nets in \mathbb{E}^3 varies in a complex manner as edge lengths grow. These effects are too complex to analyse in detail here.

5. Degree-4 examples

We have focused thus far on dense degree-3 examples. The technique is, however, more generally applicable. For example, regular, dense degree- k ribbon tilings exist in \mathbb{H}^2 for all integer values of k exceeding 2, with solutions within the Coxeter, hat and stellate classes, namely $\star 222k$, $2\star 2k$ and $222k$. Some, though not all, of those orbifolds are found as commensurate translationally periodic subgroups of the P , D , gyroid and H TPMSs. We describe here some aspects of degree-4 and degree-6 regular ribbon tilings, sufficient we hope to guide the reader to the broader universe of these patterns that we cannot cover exhaustively here. These patterns are formed by reticulating P , D and G TPMSs (degree-4 and degree-6 ribbons) and the hexagonal H surface (degree-6 ribbons).

The correspondences between two-dimensional hyperbolic orbifolds on the TPMSs and three-dimensional Euclidean space groups are listed in Appendix B. Since the degree-4 and 6 reticulations on the cubic TPMSs are subgroups of the full hyperbolic symmetries, they form tetragonal and rhombohedral patterns, respectively. (Though in some cases they can be further symmetrized in \mathbb{E}^3 without changing their entanglements, to form cubic patterns.)

Consider degree-4 examples, which result from free tilings on the P , D and gyroid TPMSs. Fig. 17 shows the degree-4 ribbon tilings in \mathbb{H}^2 that form from Coxeter and stellate orbifolds [$\star 2224$ (group 123) and 2224 (group 114)].

The $\star 2224$ orbifold contains three copies of the $\star 246$ orbifold. Whereas the degree-3 Coxeter ribbon tiling has a single embedding within the $\star 246$ discretization of \mathbb{H}^2 due to the automorphism of $\star 246$ that exchanges the two edges linking $\star 3$ and $\star 2$ sites, the degree-4 tiling has two possible embeddings, given by the two edges linking $\star 4$ and $\star 2$ sites that are not related by an automorphism. The two embeddings of the decorated $\star 2224$ orbifold into $\star 246$ are illustrated in

Fig. 17. In contrast to the degree-3 case, the hat orbifold relevant to degree-4 tilings, $2\star 24$, is forbidden in our schema, as it does not preserve the full set of translation symmetries of the cubic TPMSs.

An infinite number of degree-4 stellate tilings with orbifold 2224 are possible. That follows from generalization of the 2223 cases discussed in §3.3. The argument developed in Appendix A holds for all $222k$ orbifolds, where $k > 2$. The rotational symmetry at each k -fold vertex (analogous to Q_C) confines the location of the (Q_C) generator to a restricted radial sector {subtending an angle of $2\pi/k$ at Q_C , equivalent to inserting $[(k - 2)\pi]/k$ disclinations into the flat Euclidean plane}. Hence any $222k$ discretization of \mathbb{H}^2 has vertices Q_C and Q_A , located within a subdomain of \mathbb{H}^2 that is equivalent to the 2222 discretization of \mathbb{E}^2 within a $2\pi/k$ sector. We illustrate the first five in Fig. 17.

The embeddings of these orbifolds are illustrated in Fig. 18. As in the degree-3 case, the two covering maps of the G surface correspond to placing the hyperbolic pattern on the front or back sides (green or purple side up) of the highlighted surface domain.

A priori, these tilings must form patterns composed of regular degree-4 nets, namely 3-periodic **dia**, 2-periodic **sql**

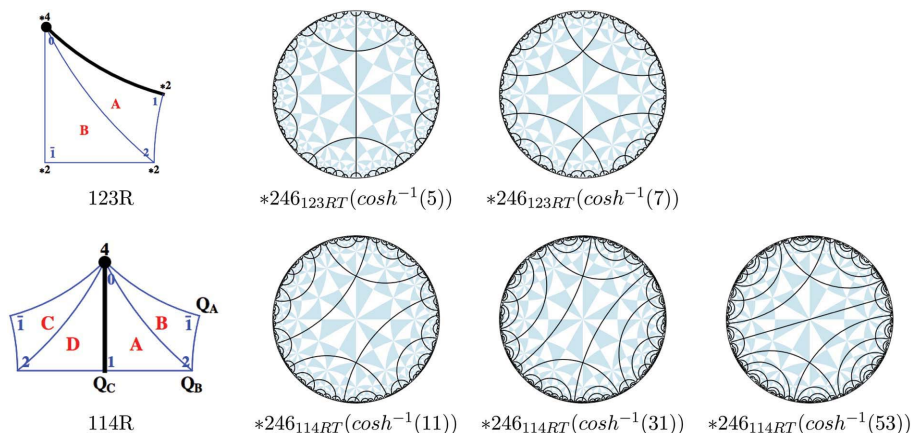


Figure 17
(Left) Delaney–Dress representations of degree-4 regular ribbon tilings of (top) $\star 2224$ and (bottom) 2224 orbifold domains (bounded by blue polygons) with vertices and edges shown in black (cf. Fig. 4). (Right) The free tilings of \mathbb{H}^2 . The first row is the Coxeter embeddings, the second illustrates the first three members of the infinite family of stellate examples.

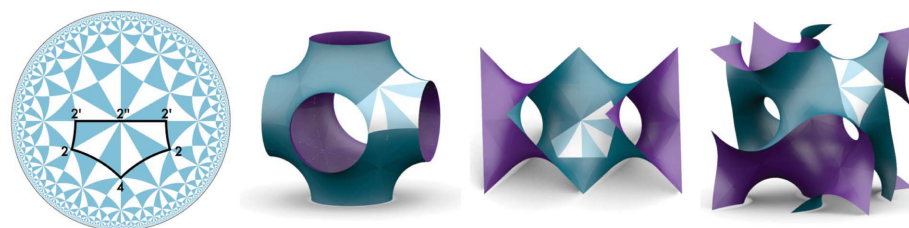


Figure 18
The correspondence between a patch in \mathbb{H}^2 and a patch on each of the surfaces is shown, for the stellate orbifold 2224 on the (left to right) P , D and G surfaces.

Table 4
Regular, dense degree-4 ribbon tilings.

See Table 1 for details.

Structure	Figure	# comp.	Topology	Notes
$P_{123RT}(\cosh^{-1}(5))$		1*	sql	Parallel array
$P_{123RT}(\cosh^{-1}(7))$		∞	4-chains	Parallel 1-periodic degree-4 chains
$P_{114RT}(\cosh^{-1}(11))$	Fig. 19	4	dia	Class IIIa, 6-6-rings: 18 Hopf links
$P_{114RT}(\cosh^{-1}(107))$	Fig. 19	4	dia	Class IIIa, 6-6-rings: 59 Hopf links, 3 higher-order links
$D_{123RT}(\cosh^{-1}(5))$		2	dia	Class IIa, 6-6-rings: 6 Hopf links
$D_{114RT}(\cosh^{-1}(11))$		2	dia	Class IIa, 6-6-rings: 6 Hopf links
$G_{123RT}(\cosh^{-1}(5))$	Fig. 20	2	dia	Class IIa, 6-6-rings: 6 Hopf links
$G_{123RT}(\cosh^{-1}(7))$		2	dia	Class IIa, 6-6-rings: 6 Hopf links

layer nets, 1-periodic 4-chains or finite **oct** (octahedral edge) nets. As in the degree-3 case, generic patterns are entangled 3-periodic nets: here **dia** nets. The patterns formed in \mathbb{E}^3 are listed in Table 4. In contrast to the degree-3 examples, finite unentangled **oct** nets are not formed among the lower-order members and a 1-periodic (4-chain) example is found.

For example, Fig. 19 shows two structures, each containing four entangled **dia** nets, whose entanglements are distinct, according to the *TOPOS* link count (Table 4).

In contrast to the degree-3 examples, the entanglements of **dia** nets are not necessarily unique for each free tiling. Fig. 20 shows an example of a reticulation on the G surface of a pair of catenated **dia** nets, which is likely equivalent to entanglements on the D and G surfaces with equivalent topology: the *TOPOS* output for these four examples is insufficient to establish the equivalence of these entanglements, since distinct ambient isotopic classes may have identical output. Other approaches are needed (and one possible route is discussed below). In these cases, however, it is clear that the edges can, in all cases, be straightened without edges passing through each other to form what is, by inspection, most likely a common entanglement of two **dia** nets.

6. Degree-6 examples

Regular, dense ribbon tilings of \mathbb{H}^2 can be constructed on $\star 2226$, $2\star 26$ and 2226 orbifolds. These cases are worth cursory description as they can be realized on both cubic TPMSs and the hexagonal H surface. Tilings of the latter TPMS have not been systematically developed to date. For example, the online catalogue of tilings, *Epinet*, has so far analysed only Coxeter tilings of the P , D and G surfaces (Hyde *et al.*, 2010).

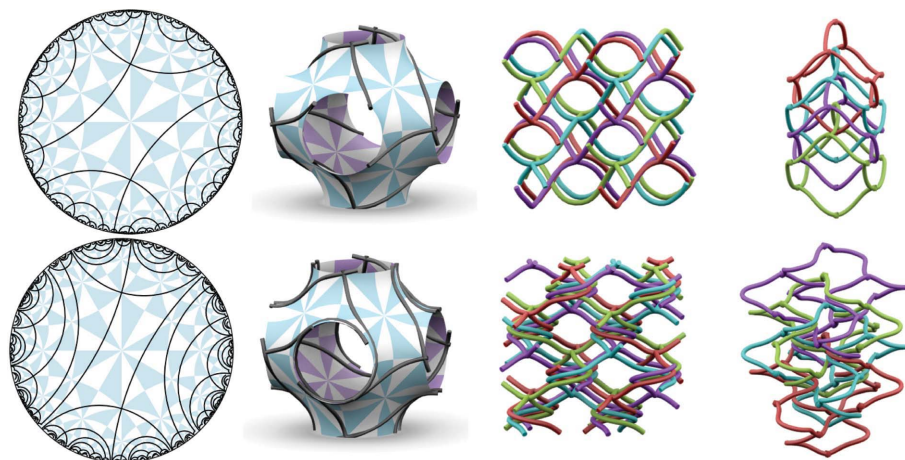


Figure 19
 (Top) The stellate (2224) tiling $P_{114RT}(\cosh^{-1}(11))$ that forms four catenated **dia** nets. (Bottom) Another stellate pattern, $P_{114RT}(\cosh^{-1}(107))$, also contains four interpenetrating components of **dia**. Single adamantane cages of each disjoint component are also illustrated. These are not equivalent entanglements.

The hexagonal genus-3 TPMS, discovered by Schwarz and known as the *H* surface (Schoen, 1970), has two-dimensional orbifold $\star 2226$, as shown in Fig. 21 (Hyde, Ramsden *et al.*, 2003). A list of two-dimensional groups that conserve all translational isometries of the surface has been determined (Robins *et al.*, 2004*b*). In contrast to the cubic examples above, the *H* surface embeds in \mathbb{E}^3 with a one-parameter family of lattices, characterized for example by the ratio of *c/a* parameter for the hexagonal unit cell. This flexibility is found too in the two-dimensional group, since the shape of the $\star 2226$ orbifold itself has one degree of freedom (Hyde, Ramsden *et al.*, 2003).

In common with the degree-4 Coxeter example ($\star 2224$) on the cubic TPMSs, two distinct degree-6 Coxeter ribbon tilings can be constructed on the *H* surface with a symmetry group of $\star 2226$ (Fig. 23). This orbifold cannot be realized on the cubic TPMSs. Among the subgroups of the Coxeter $\star 2226$ pattern related to dense, regular ribbon tilings, analogous to the degree-3 and 4 cases discussed above, the hat orbifold ($2\star 26$) also contains all the full translation subgroups of the *P*, *D* and *G* surfaces (Robins *et al.*, 2004*a*), though it is not commensurate with translations of the *H* surface. The related stellate orbifold (2226) maps onto the cubic and hexagonal surfaces,



Figure 20
 The Coxeter ($\star 2224$) tiling $G_{123RT}(\cosh^{-1}(5))$ forms a pair of catenated **dia** nets.

affording a wealth of potential patterns (Robins *et al.*, 2004*a,b*). One possible embedding of this orbifold in the cubic and hexagonal surfaces is illustrated in Fig. 22.

Projection of these degree-6 tilings must result in multiple regular nets of degree-6 in \mathbb{E}^3 , with exactly two vertices per translational unit cell of each of the TPMSs. Possible net topologies are 3-periodic **pcu**, 2-periodic **hxl** components, arrays of 1-periodic chains of degree-6 vertices (6-chains) or finite (non-simple) graphs with two vertices of degree-6. The nets that emerge are listed in Table 5. The edge-length calculations for the *H* surface tilings are complicated by the degree of freedom in the $\star 2226$ domain, as this implies that the edge lengths are not uniquely defined. We work around this by giving

an edge length for the symmetrized $\star 2226$ domain to be a gluing of the $\star 24(12)$ tiling (giving the quadrilateral domains illustrated in Fig. 22), for which the edges are uniquely defined. However, the symmetrization means that there are often two distinct tilings with the same edge length, thus we distinguish these with a further number 1 or 2.

As in the degree-3 and 4 cases, the predominant patterns contain multiple 3-periodic nets; here consisting of **pcu** components, though 2-periodic **hxl** nets and 1-periodic 6-chains are also generated, as shown in Fig. 23.

In contrast to the lower-degree tilings, the degree-6 ribbon tilings also yield examples of 3-periodic nets containing just a single component (Fig. 24). These single-component **pcu** structures [$P_{93RT}(\cosh^{-1}(15))$, $D_{93RT}(\cosh^{-1}(15))$ and $G_{93RT}^+(\cosh^{-1}(15))$] are equivalent by ambient isotopy to the usual (untangled) barycentric embedding of **pcu**. Other regular tilings of the cubic surfaces consist of two interpenetrating **pcu** components that are equivalent entanglements [$P_{122RT}(\cosh^{-1}(17))$ (Fig. 24), $D_{122RT}(\cosh^{-1}(49))$ and $G_{122RT}(\cosh^{-1}(17))$].

The $D_{93RT}(\cosh^{-1}(63))$ and $G_{122RT}(\cosh^{-1}(49))$ patterns contain four **pcu** components and are also distinct entanglements. The *H* surface structures [$H_{31RT}(\cosh^{-1}(26.9))$ and

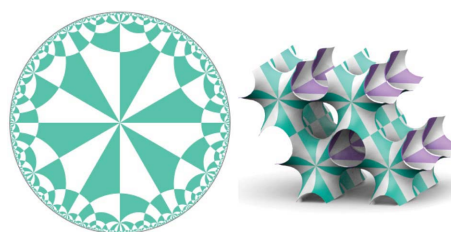


Figure 21
 (Left) The Coxeter $\star 2226$ tiling of \mathbb{H}^2 represented on the Poincaré disc model. (Right) The *H* minimal surface decorated by the same tiling. Each tile defines an asymmetric patch on the surface and tile edges are mirror lines.

Table 5

Regular, dense degree-6 ribbon tilings.

See Table 1 for details.

Structure	Figure	# comp.	Topology	Notes
$H_{32RT}(\cosh^{-1}(13.9) : 1)$	Fig. 23	∞	6-chains	Parallel 1-periodic 6-chains
$H_{32RT}(\cosh^{-1}(13.9) : 2)$	Fig. 23	1*	hxl	Parallel array
$H_{31RT}(\cosh^{-1}(26.9))$	Fig. 25	3	pcu	Class Ia 4-4-rings: 8 Hopf links. 4-6-cycles: 36 Hopf links. 6-6-cycles: 40 Hopf links
$H_{31RT}(\cosh^{-1}(154.9) : 2)$	Fig. 25	3	pcu	Class Ia 4-4-rings: 20 Hopf links. 4-6-cycles: 90 Hopf links. 6-6-cycles: 86 Hopf links and 2 higher-order links
$P_{122RT}(\cosh^{-1}(17))$	Fig. 24	2	pcu	Class IIa 4-4-rings: 4 Hopf links. 4-6-cycles: 24 Hopf links. 6-6-cycles: 40 Hopf links
$P_{93RT}(\cosh^{-1}(15))$		1	pcu	
$D_{122RT}(\cosh^{-1}(49))$		2	pcu	Class IIa 4-4-rings: 4 Hopf links. 4-6-cycles: 24 Hopf links. 6-6-cycles: 40 Hopf links
$D_{93RT}(\cosh^{-1}(15))$		1	pcu	
$D_{93RT}(\cosh^{-1}(63))$		4	pcu	Class Ib 4-4-rings: 12 Hopf links. 4-6-cycles: 66 Hopf links. 6-6-cycles: 74 Hopf links and 1 higher-order link
$G_{122RT}(\cosh^{-1}(17))$		2	pcu	Class IIa 4-4-rings: 4 Hopf links. 4-6-cycles: 24 Hopf links. 6-6-cycles: 40 Hopf links
$G_{122RT}(\cosh^{-1}(49))$	Fig. 24	4	pcu	Class IIIa 4-4-rings: 12 Hopf links. 4-6-rings: 72 Hopf links. 6-6-rings: 120 Hopf links
$G_{93RT}(\cosh^{-1}(15))$		1	pcu	

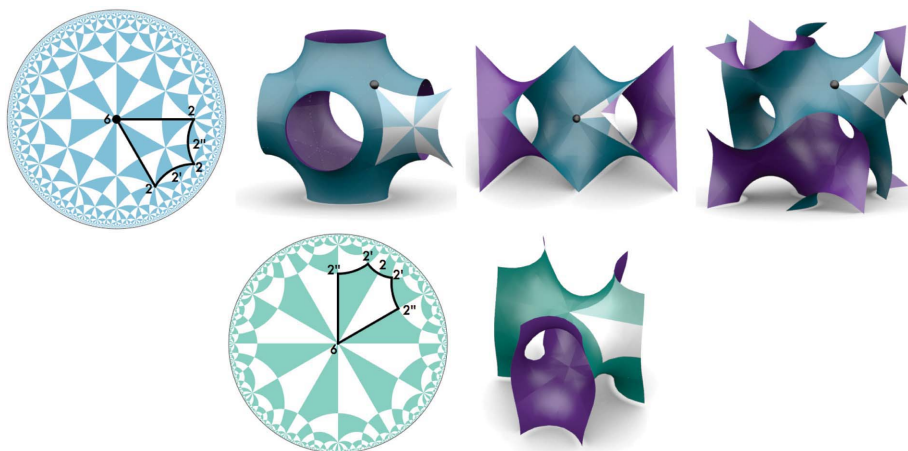


Figure 22

The correspondence between a single copy of the stellate 2226 orbifold in \mathbb{H}^2 and a patch on the TPMS. (Top, from left to right) P , D and G surfaces. (Bottom) H surface.

$H_{31RT}(\cosh^{-1}(154.9) : 2)$ form patterns containing three interpenetrating **pcu** nets that are distinct entanglements, illustrated in Fig. 25.

7. Towards canonical embeddings of entangled nets

The powerful concept of barycentric placement, developed by Delgado-Friedrichs & O’Keeffe (2003), can be used to form a geometric realization of a net – an embedding in \mathbb{E}^3 – from its topology alone. That approach effectively ‘untangles’ any net embedding formed on a TPMS, giving an embedding with straight edges (Hyde & Delgado-Friedrichs, 2011; Castle *et al.*, 2011). In mathematical terms, the ambient isotopy class of the net embedding on the TPMS is not necessarily the same as that given by a barycentric embedding.³ In practical terms, this means that an embedding *via* barycentric placement may have different edge crossings than the original edge pattern on the TPMS, and the process of straightening the edges requires edges to pass through each other to form the relaxed

³ Any embedding of the abstract ‘barycentric placement’ is equivalent, since the embeddings are all equivalent within an affine transformation (Delgado-Friedrichs & O’Keeffe, 2003), which conserves ambient isotopy.

embedding induced by barycentric placement. This standard embedding therefore, while indispensable to characterization of a net topology, does not characterize (or preserve) entanglement. Entanglement of many components is a more subtle concept still.

A recent paper offers partial resolution of this issue for multiple nets, allowing numerical signatures for simpler entanglements, containing links (Alexandrov *et al.*, 2012). This approach, while useful, is unable to classify generic patterns whose entanglements are not necessarily induced by links. We describe here a novel approach that allows entanglement to

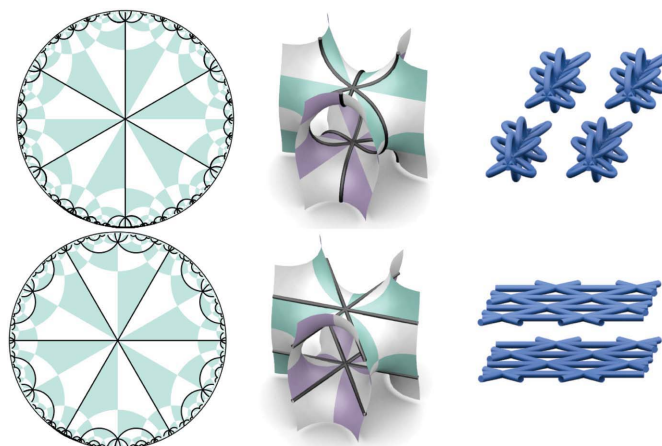


Figure 23

(Top) One Coxeter ($\star 2226$) $H_{32RT}(\cosh^{-1}(13.9) : 1)$ degree-6 regular, dense ribbon tiling in \mathbb{H}^2 , on the H surface and in \mathbb{E}^3 (from left to right). The Euclidean embedding consists of parallel 1-periodic 6-chains. (Bottom) The second $\star 2226$ $H_{32RT}(\cosh^{-1}(13.9) : 2)$ tiling, which forms parallel layers of 2-periodic **hxl** nets.

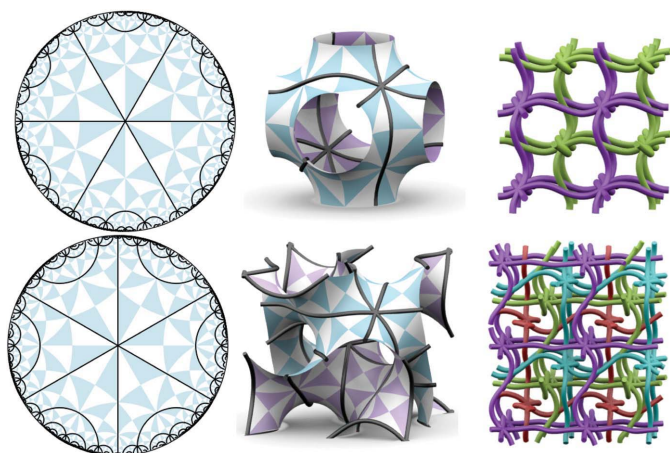


Figure 24
 (Top) The hat $(2\star 26) P_{122RT}(\cosh^{-1}(17))$ degree-6 regular, dense ribbon tiling shown in \mathbb{H}^2 , on the P surface and in \mathbb{E}^3 (from left to right). The Euclidean pattern consists of two interpenetrating components of **pcu**. (Bottom) The $G_{122RT}(\cosh^{-1}(49))$ tiling that forms four interpenetrating **pcu** nets.

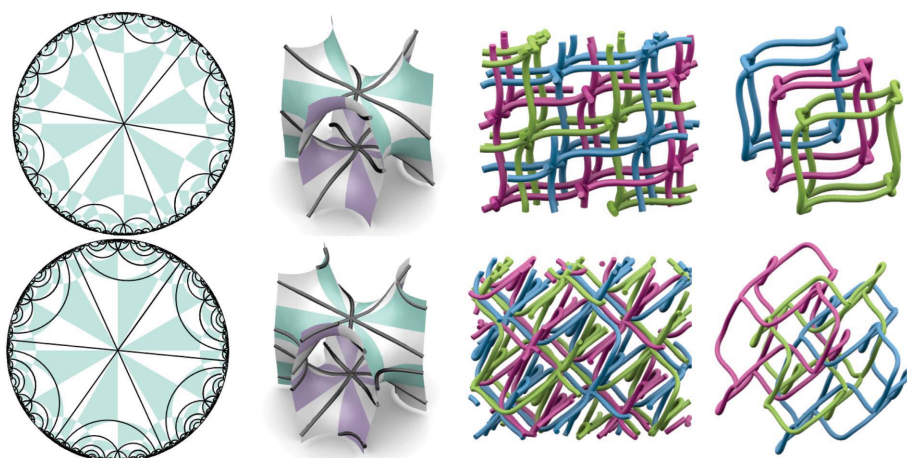


Figure 25
 (Top) An $H_{31RT}(\cosh^{-1}(26.9))$ regular, dense stellate (2226) ribbon tiling (2226) in \mathbb{H}^2 , on the H surface and in \mathbb{E}^3 (from left to right), where it forms three interpenetrating **pcu** nets. (Bottom) A higher-order 2226 tiling $[H_{31RT}(\cosh^{-1}(154.9) : 2)]$ that also builds three interpenetrating **pcu** nets. Single **cu** nets excized from each component are shown for each pattern, revealing distinct entanglements, confirmed by *TOPOS* link analyses.

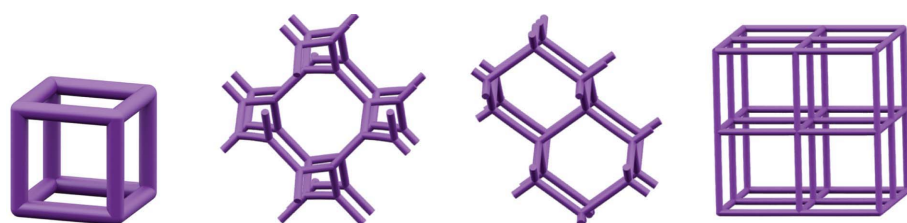


Figure 26
 Ideal embeddings of untangled isotopes of the **cu**, **srs**, **dia** and **pcu** nets found numerically using the PB-SONO algorithm. The diameter of edges of the ideal structure has been decreased in all cases to illustrate their edge geometry: the true ideal embedding has maximally inflated edges.



Figure 27
 Ideal embeddings of two tangled isotopes of the **cu** net.

be effectively geometrized, just as barycentric placement leads to a useful geometrical realization of a net topology.

Our approach builds on the concept of a ‘tight embedding’ from knot theory that often – though by no means always – affords a unique and therefore canonical embedding for conventional knots and links (Stasiak *et al.*, 1998). Tight or ‘ideal’ embeddings of knots are formed as follows. The algorithm searches for knot conformations that minimize the knot length for a given diameter (L/D). Assume all filaments have a fixed diameter, D , that filaments can never overlap except along lines or at isolated points (they touch tangentially) and that they have infinite flexibility and zero friction. These assumptions are easily implemented numerically. The ‘ideal’ or ‘tight’ configuration of the knot is that which minimizes the ratio L/D . A fast and effective algorithm for finding this minimum is the SONO algorithm (Pieranski, 1998).

Here we extend this notion to find ideal embeddings of (multiple) nets. To do this, we generalize the SONO algorithm to allow for periodic boundary conditions and minimize L/D within one unit cell. Some further extensions of the SONO algorithm are required to allow tightening of multiple nets, owing to the presence of branched vertices.

This adapted algorithm is explored in detail in Evans (2011) and we refer to it as PB-SONO throughout this paper. The PB-SONO algorithm forms embeddings of simple knots that are very similar to those found with the simpler SONO algorithm, shown by comparable L/D values (Evans, 2011). Further, tightening of arbitrary (untangled) isotopes of regular single-component nets by PB-SONO forms high-symmetry patterns, as expected. (Some discrepancies are unavoidable due to the vertices, where edges must overlap; however these can be effectively removed by judicious discretization of the net edges.) Some examples are shown in Fig. 26. These ideal embeddings correspond (within the numerical uncertainty of the algorithm) to the most symmetric embeddings of these regular nets (*i.e.* symmetrically identical edges and vertices).

In contrast, tangled isotopes form geometrically distinct embeddings in \mathbb{E}^3 after tightening with PB-SONO. Fig. 27 shows two ideal embeddings of tangled cube isotopes, discussed in detail in Hyde & Schröder-Turk (2007). Clearly, these isotopes adopt distinct embeddings and differ from the untangled isotope embedding.

These examples have unique tightest configurations, thereby allowing canonical embeddings of isotopes that respect both their topology and entanglement. In general, uniqueness is not assured (an unfortunate feature that is also observed in classical links; Cantarella *et al.*, 2002). However, this approach affords a very useful ‘canonical’ embedding for the multiple nets formed from ribbon tilings.

Consider tightening multiple nets from starting embeddings formed by the TPMS reticulations. For example, ideal embeddings of 4 and 8 **srs** nets from the $D_{124RT}(\cosh^{-1}(3))$ and $P_{129RT}(\cosh^{-1}(5))$ ribbon tilings are illustrated in Fig. 28.

These embeddings afford useful and reasonable canonical configurations for these entanglements of (untangled) **srs** nets. For example, the **srs** nets in both of these tight embeddings are regular, adopting the familiar symmetrized (barycentric) form of cubic **srs**.

Similarly, tight embeddings of multiple **pcu** and **dia** (untangled) isotopes converge to embeddings whose individual component nets are also regular, as shown in Fig. 29.

This may appear a very convoluted route to embedding multiple nets. Indeed, many of these multiple **srs**, **dia** and **pcu** nets have already been described by Wells (1977) and others, and catalogued by O’Keeffe *et al.* (2008). However, these examples, while not novel, illustrate the utility of the tightening approach in forming canonical embeddings of multiple nets.

The approach is most powerful when analysing novel entanglements, a situation that has not been considered to date by structural chemists. Consider, for example, the pair of **srs** nets that result from the $G_{124RT}(\cosh^{-1}(3))$ and $G_{129RT}(\cosh^{-1}(5))$ ribbon tilings (shown in Figs. 11, 12). Tightening of those patterns using the PB-SONO algorithm results in two very distinct embeddings, even though both patterns consist of a pair of interwoven **srs** nets. The ideal embeddings are shown in Fig. 30. Here the tightening algorithm offers two useful results. First, the geometric differences between these

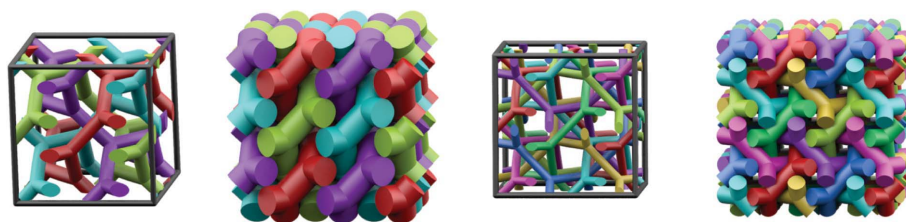


Figure 28

Ideal embeddings of multiple (like-handed) **srs** nets. (Left to right) Four **srs** nets from the $D_{124RT}(\cosh^{-1}(3))$ tiling and eight **srs** nets from the $P_{129RT}(\cosh^{-1}(5))$ tiling, shown both within one unit cell to show detail and as a repeated pattern.

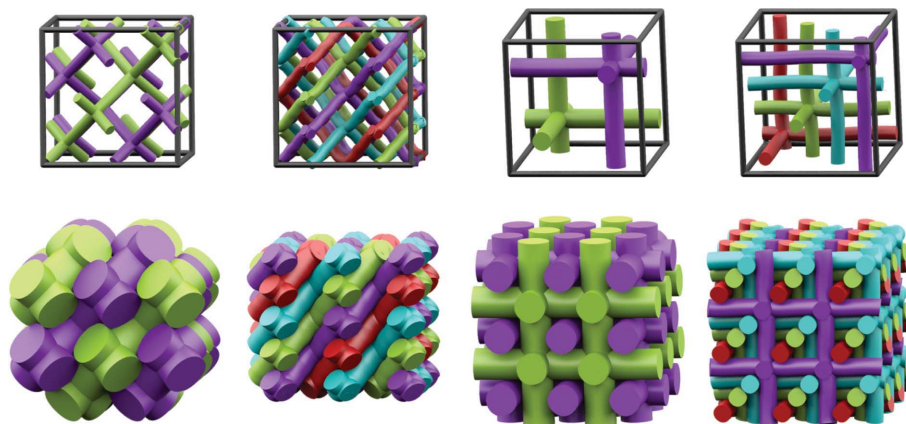


Figure 29

Ideal embeddings of untangled isotopes of multiple **dia** and **pcu** nets. (Left to right) Two **dia** nets from the $D_{123RT}(\cosh^{-1}(5))$ tiling; four **dia** nets from the $P_{114RT}(\cosh^{-1}(11))$ tiling; two **pcu** nets from the $P_{122RT}(\cosh^{-1}(17))$ tiling; and four **pcu** nets from the $G_{122RT}(\cosh^{-1}(49))$ tiling. The upper images show one unit cell of the pattern and the lower images the global pattern.

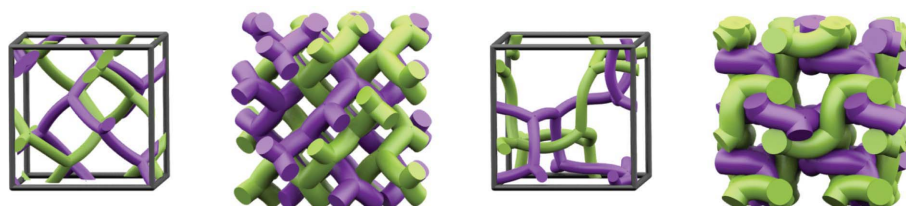


Figure 30

(Left to right) Ideal embeddings of untangled isotopes that form from the $G_{124RT}(\cosh^{-1}(3))$ and $G_{129RT}(\cosh^{-1}(5))$ tilings. Both patterns contain a pair of (like-handed) **srs** nets.

two tight embeddings confirm that they are distinct entanglements. Second, the algorithm gives a canonical embedding of the new entangled pattern that emerges from the $G_{129RT}(\cosh^{-1}(5))$ tiling. Interestingly, the crystallographic data from a synthesized pair of **srs** nets with equivalent chirality given in Kepert *et al.* (2000) give a conformation that matches the ideal form of the $G_{124RT}(\cosh^{-1}(3))$ structure, which suggests that these ideal conformations are relevant for chemical frameworks.

The examples shown here are among the simpler patterns. In many of these cases, a combination of the *TOPOS* and *GAVROG* algorithms allows distinct patterns (with distinct topologies and/or entanglements) to be distinguished. However, since *TOPOS* can only analyse simpler entangle-

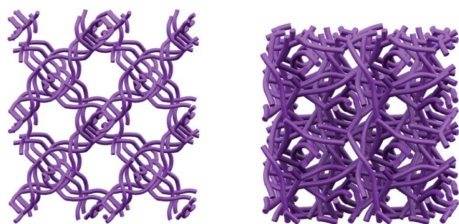


Figure 31

The ideal embeddings of one component of each of the $G_{118RT}^-(\cosh^{-1}(195))$ (left) and $G_{118RT}^+(\cosh^{-1}(195))$ (right) structures. The ideal embeddings of both networks are distinct and different to the untangled embedding of **srs** (Fig. 26). Therefore all three **srs** nets are distinct isotopes and the two shown here are tangled.

ments and *GAVROG* identifies net topology rather than entanglement, generic patterns cannot be well characterized by these approaches. The PB-SONO algorithm provides an additional tool for the cases where the other algorithms fail.

7.1. Entangled embeddings of tangles

An additional phenomenon is possible in multiple nets and present in some higher-order stellate ribbon tilings. That is the possibility of entangled nets that are themselves tangled. Recall that ‘untangled’ nets are ambient isotopic to a barycentric embedding (Castle *et al.*, 2011). Self-entangled nets (also known as self-catentated, self-penetrated or self-knotted) can then be defined with respect to this untangled ‘ground state’, by analogy with the unknotted state of knots, namely an embedding of a simple unthreaded loop in \mathbb{E}^3 . Self-entangled net embeddings cannot be transformed into the untangled barycentric embedding without ‘phantom crossings’, where edges pass through each other.⁴ For example, both $G_{118RT}^-(\cosh^{-1}(195))$ and $G_{118RT}^+(\cosh^{-1}(195))$ patterns contain two **srs** networks. If we take a single component of these structures and relax using the PB-SONO algorithm, we find that these single nets are tangled, since their ideal embeddings (Fig. 31) are different from the untangled **srs** ideal embedding (Fig. 26). Further, since both ideal embeddings are geometrically distinct, these are distinct isotopes. Clearly, entangled embeddings of nets that are themselves tangled are possible, as well as the presence of more complex entanglements beyond knotted and linked cycles, such as ravels (Castle *et al.*, 2008; Li *et al.*, 2011).

8. Conclusion

We have constructed and characterized a number of intergrown regular nets. Our approach introduces the notion of ‘free tilings’ of two-dimensional hyperbolic space (\mathbb{H}^2) and then maps those patterns into three-dimensional Euclidean space (\mathbb{E}^3) to form a variety of patterns composed of multiply

⁴ This terminology is perhaps misleading, since everyday tangles, from rope to earphone leads, are usually ambient isotopic to the untangled state, and untangling does not require phantom crossings (or cuts), as the patient fisherman knows. Our tangled nets are perhaps better described as ‘knotted’. However, since all nets contain knots, we prefer the ‘tangled’ descriptor to distinguish knots within nets from knotted nets.

entangled regular nets. Those maps are the so-called covering maps from \mathbb{H}^2 to four genus-3 TPMSs, the (cubic) *P*, *D*, *G* and (hexagonal) *H* surfaces. Here we have explored in some detail one variety of free tilings, composed of ribbon tiles. The Euclidean patterns that emerge are commonly made up of 3-periodic nets that arise frequently in synthetic chemical frameworks (Batten & Robson, 1998; O’Keeffe *et al.*, 2000). We suspect that more complex examples of such nets will emerge in the future in a variety of materials. We note, for example, that the most common nets in MOFs include the trio of 3-periodic nets – **srs**, **dia** and **pcu** – that are the predominant components of regular ribbon tilings (Ockwig *et al.*, 2005; Blatov *et al.*, 2004; Alexandrov *et al.*, 2011). Furthermore, intergrowths of those nets are very common in MOF materials (Batten & Robson, 1998; Delgado Friedrichs *et al.*, 2003; Reineke *et al.*, 2000; Wu *et al.*, 2011). This paper has focused on examples that emerge from regular hyperbolic free tilings, yielding the most symmetric and simplest patterns accessible by this technique.

The scope for further enumeration of structures of this kind is large. The free tilings of \mathbb{H}^2 that have been considered here are a fraction of all possible tilings of this kind. Three directions are immediately apparent: firstly, enlargement of the current enumeration to include higher-order regular ribbon tilings (in the stellate class); secondly, to move beyond patterns that emerge from close-packed trees in \mathbb{H}^2 ; and thirdly, to extend the analysis to less regular patterns on \mathbb{H}^2 . In addition, we have somewhat arbitrarily delimited our enumeration to those cases that give 3-periodic patterns whose translation groups are identical to those of the *P*, *D*, *G* and *H* TPMSs. That constraint can be removed without significant complication, if one is prepared to accommodate the resulting combinatorial explosion. In addition, ribbon tilings commensurate with other TPMSs can be constructed.

These hyperbolic ribbon tilings have natural dual patterns, whose tiles are themselves tree-like, and are bounded by an unbounded number of vertex-free (hyperbolic) lines. Those tilings result in three-dimensional packing of one-dimensional ‘filaments’ in \mathbb{E}^3 (Evans & Hyde, 2011). Hybrid free tilings, with both branched boundary components and infinite geodesic boundary components, are also possible in \mathbb{H}^2 . These form intergrowths of nets and filaments in \mathbb{E}^3 (Castle *et al.*, 2011). The companion paper to this one is focused on filament packings (Evans *et al.*, 2013).

APPENDIX A Embedding of stellate orbifolds

In contrast to the Coxeter and hat cases, stellate orbifolds, which contain rotation centres, have an unlimited number of embeddings within the $\star 246$ setting. The stellate case leads to a two-parameter family of orbifold domains. Possible locations of the orbifold domain are confined to a Euclidean subset of \mathbb{H}^2 , discretized by $\mathbb{Z} \times \mathbb{Z}$. We describe the reasons for that here.

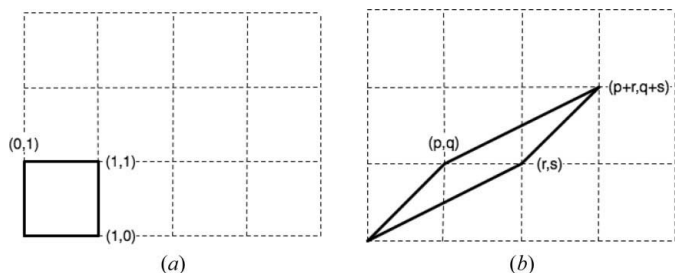


Figure 32
 (a) An embedding of the 2222 orbifold in \mathbb{E}^2 . The corners of the square coincide with the points $\{0, 0\}$, $\{1, 0\}$, $\{1, 1\}$ and $\{0, 1\}$, establishing a reference frame of $\mathbb{Z} \times \mathbb{Z}$ for subsequent embeddings. (b) Another embedding of 2222 relative to the established reference frame.

It is convenient here to consider all possible coverings of the generic stellate orbifold of the form 222k into its universal cover (\mathbb{E}^2 if $k = 2$ and \mathbb{H}^2 if $k > 2$). We wish to systematically generate all distinct coverings of the 222k orbifold into the covering plane.

Consider first the 2^4 (2222) orbifold, which covers \mathbb{E}^2 . The covering is determined by the choice of the four distinct twofold rotation sites that are the group generators. Fig. 32(a) shows a covering where the generators are at the positions $\{0, 0\}$, $\{1, 0\}$, $\{1, 1\}$ and $\{0, 1\}$ of \mathbb{E}^2 . In this case, *all* rotation centres of the infinite group are centred at integer coordinates. Labelling the twofold rotation centres located at $\{0, 0\}$, $\{1, 0\}$, $\{1, 1\}$ and $\{0, 1\}$ as Q_T , Q_A , Q_B and Q_C , respectively, the presentation of the group given by the reference frame is

$$\langle \{Q_T, Q_A, Q_B, Q_C\} : (Q_A)^2 = (Q_B)^2 = (Q_C)^2 = (Q_T)^2 = I, Q_T = Q_A Q_B Q_C \rangle.$$

Distinct presentations of the same group may be obtained by defining new generators, Q'_T , Q'_A , Q'_B and Q'_C , whose forms are words of the simpler group (Q_T , Q_A , Q_B and Q_C) (Coxeter & Moser, 1972).

A set of possible coverings may be represented through parallelograms superimposed on the rectilinear $\mathbb{Z} \times \mathbb{Z}$ grid. To preclude duplication of coverings, we consider only one quadrant of \mathbb{E}^2 and fix the twofold rotation Q_T . We require that the only isometries of the parallelograms are the twofold rotations at their vertices consistent with the satellite orbifold. Further, we impose a condition that will be needed for all non-Euclidean cases ($k \neq 2$), namely that parallelograms must have area 1 (*i.e.* equal in area to the initial reference embedding). In \mathbb{H}^2 , this condition is imposed by the fact that the area of an orbifold 222k scales as $(k - 2)/k$ and is fixed for fixed k . (Note that this quadrilateral domain enclosed by the four distinct twofold rotations is a half of a single 2222 domain; the full domain has area 2.) These restrictions on placement of generators are equivalent to satisfying the group relations for a covering. Fig. 32(b) shows an example of a unit area parallelogram on $\mathbb{Z} \times \mathbb{Z}$ with corners $\{0, 0\}$, $\{r, s\}$, $\{p + r, q + s\}$ and $\{p, q\}$. Each grid point in the plane represents elements of the infinite group, hence we may express the corner points of the parallelogram (with respect to the reference frame) as

$$\begin{aligned} Q'_A &= Q_B Q_C Q_B, & Q'_C &= Q_B, \\ Q'_B &= Q_B Q_C Q_B Q_A Q_B Q_C Q_B, & Q'_T &= Q_T. \end{aligned}$$

Since the new generators remain twofold rotation centres, the group relations $(Q'_A)^2 = (Q'_B)^2 = (Q'_C)^2 = (Q'_T)^2 = I$ are satisfied. The other group relation, where $Q'_A Q'_B Q'_C$ must be equal to Q'_T , is also satisfied, hence the generators Q'_T , Q'_A , Q'_B and Q'_C are a covering of the symmetry group of the 2222 orbifold. An analogous argument holds for all other parallelogram vertices satisfying the constraints listed above.

To ensure that no additional symmetry points are located on the boundary of the parallelogram, the Q'_C vertex ($\{p, q\}$) of the parallelogram is chosen such that $\{p, q\}$ are coprime. Coordinates of the opposite Q'_A vertex, $\{r, s\}$, are chosen such that the parallelogram has unit area. The area constraint implies that $ps - rq = 1$, giving three degrees of freedom for all coverings of 2222 into \mathbb{E}^2 (Castle *et al.*, 2012).

This Euclidean case is readily generalized to hyperbolic orbifolds of the form 222k (where $k > 2$). Those orbifolds tile \mathbb{H}^2 rather than \mathbb{E}^2 . Consider, for example, the $k = 3$ case. As above, we first choose a specific embedding of the orbifold, our reference frame in \mathbb{H}^2 , which consists of the four group generators: Q_T , Q_A , Q_B and Q_C (Fig. 33a). The group relations for the 2223 symmetry group are given by

$$\langle \{Q_T, Q_A, Q_B, Q_C\} : (Q_A)^2 = (Q_B)^2 = (Q_C)^2 = (Q_T)^3 = I, Q_T = Q_A Q_B Q_C \rangle.$$

Fig. 33(b) shows an alternative quadrilateral whose vertices are elements of the infinite group 2223. To establish if these vertices (Q'_A , Q'_B , Q'_C and Q'_T) are alternative rotation centres that generate the same group, and hence if the new quadrilateral is a valid embedding of the group, we consider the group relations. By analogy with the Euclidean case, these vertices may be expressed in terms of the reference quadrilateral as follows:

$$\begin{aligned} Q'_A &= Q_B Q_C Q_B, & Q'_C &= Q_B, \\ Q'_B &= Q_B Q_C Q_B Q_A Q_B Q_C Q_B, & Q'_T &= Q_T. \end{aligned}$$

Once again, it is straightforward to see that the group relations $(Q'_A)^2 = (Q'_B)^2 = (Q'_C)^2 = (Q'_T)^3 = I$ are satisfied for these elements. The other group relation, where $Q'_A Q'_B Q'_C$ must be equal to Q'_T , is also satisfied; hence the quadrilateral shown

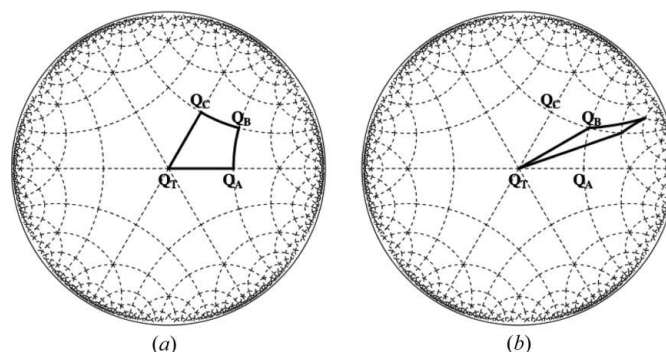


Figure 33
 (a) An embedding of the 2223 orbifold into \mathbb{H}^2 . The corners of the quadrilateral are a reference frame grid for other embeddings. (b) A subsequent embedding of the 2223 orbifold into \mathbb{H}^2 relative to the reference frame established previously. The regions shown illustrate the four rotation centres that define the group generators, and the full fundamental domains are double the size of these regions.

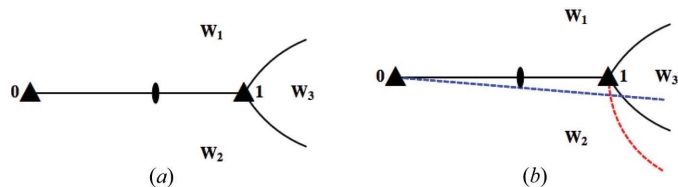


Figure 34
 (a) A diagram showing the threefold rotation at the origin (\blacktriangle_0) and an image (\blacktriangle_1), due to the twofold operation at Q_C (small black lens), where \blacktriangle_1 divides \mathbb{H}^2 into three sectors, W_1 , W_2 and W_3 . (b) If Q'_C (the end of the blue geodesic) is located in the W_3 sector, the edge from the origin to Q'_C (the blue geodesic) will certainly intersect an image of itself, as shown by the red geodesic.

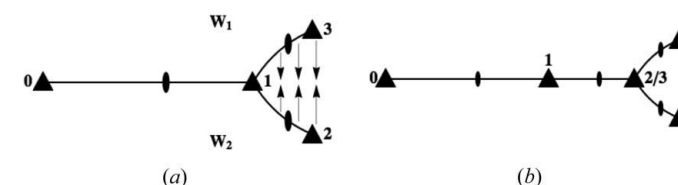


Figure 35
 (a) The sector W_3 can be excized and the boundary sewn together to form a boundary-free plane. (b) The result is a line of twofold rotations, terminating at a new threefold rotation. Repeating the cutting process further removes territory from where Q'_C is prohibited.

leads to a valid covering of the 2223 orbifold in \mathbb{H}^2 given the reference frame.

To enumerate coverings, we determine possible locations of the Q'_C generator with respect to the reference frame: the analogue of finding the coprime $\{p, q\}$ vertex of the parallelogram. We fix the Q_T generator (our origin), and consider a $\pi/3$ sector of the plane, as all others will be equivalent by symmetry (as was the case for the $\pi/2$ sector of 2222 in \mathbb{E}^2). Since a single asymmetric domain of the orbifold – the quadrilateral – necessarily tessellates \mathbb{H}^2 by the group isometries, the orbit of the quadrilateral edge from the origin to Q'_C cannot include edges that intersect the edge at some interior point.

Consider a threefold rotation site located at the origin (Q'_T), \blacktriangle_0 , in Fig. 34(a), along with its image due to the twofold operation at Q_C denoted \blacktriangle_1 . Because of the twofold isometry

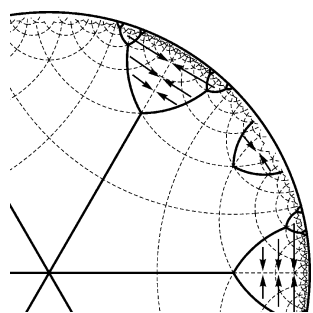


Figure 36
 Prohibited sectors of the 2223 discretization of \mathbb{H}^2 are shown. There are infinitely many prohibited sectors, located at every threefold rotation of the discretization, but only three such sectors are shown here. The remaining 'allowed' domain is a Euclidean subdomain of \mathbb{H}^2 .

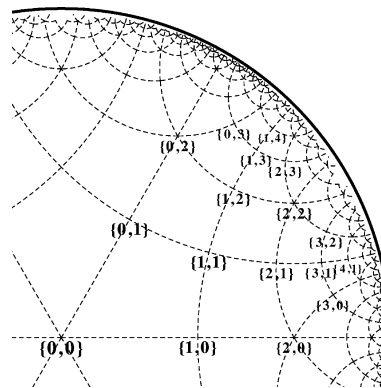


Figure 37
 The positioning of the grid points of $\mathbb{Z} \times \mathbb{Z}$ in a $\pi/3$ sector of 2223 discretization of \mathbb{H}^2 .

at Q_C , the edge from Q'_T to Q'_C in the parallelogram of the new covering must have three copies radiating from the site \blacktriangle_1 , one in each of the sectors W_1 , W_2 and W_3 . Therefore if Q'_C lies within the sector W_3 , as shown by the blue geodesic in Fig. 34(b), it necessarily intersects an image of itself radiating from \blacktriangle_1 , signified by the red geodesic in Fig. 34(b). This prohibits the placement of Q'_C in the sector W_3 .

Since the W_3 sector cannot contain Q'_C , we can excize this prohibited sector (to infinity) from \mathbb{H}^2 and fuse the pair of boundary edges of sector W_3 radiating from \blacktriangle_1 , as in Fig. 35(a). [The operation inserts a positive ($2\pi/3$) disclination at \blacktriangle_1 .] The modified domain, shown in Fig. 35(b), no longer has a threefold rotation at \blacktriangle_1 , which is now a twofold rotation, and the threefold rotations \blacktriangle_2 and \blacktriangle_3 have been fused.

By the same argument, further W_3 sectors of the plane can be excized, and a $2\pi/3$ disclination inserted at the fused $\blacktriangle_{2/3}$ site, and so on. The continued application of this process results in an infinite line of twofold rotations located at the former threefold sites. The symmetry of the remaining domain of allowed locations of Q'_C is therefore 2222, an isometry of the Euclidean plane. In other words, this sector of \mathbb{H}^2 is completely decurved by the disclinations, forming a region of \mathbb{E}^2 . These prohibited sectors are shown on the 2223 discretization of \mathbb{H}^2 in Fig. 36.

Possible locations of Q'_C are therefore confined to discrete sites in \mathbb{H}^2 , discretized by $\mathbb{Z} \times \mathbb{Z}$. By the same argument, Q'_A is likewise limited to lying within a subset of \mathbb{H}^2 whose domain is described by the pair of indices from $\mathbb{Z} \times \mathbb{Z}$ that, if fused along all boundary lines, forms a sector of \mathbb{E}^2 . (Recall lastly, that the location of Q'_B is completely determined by Q'_A and Q'_C .)

As a result of this Euclidean subdomain of \mathbb{H}^2 , we may index all possible quadrilateral domains of the 2223 orbifold exactly by parallelograms of unit area in $\mathbb{Z} \times \mathbb{Z}$. Fig. 37 shows the $\mathbb{Z} \times \mathbb{Z}$ grid within a $\pi/3$ sector of the discretization of \mathbb{H}^2 by the 2223 reference frame covering.

In contrast to the Coxeter and hat orbifolds, the stellate case therefore leads to a two-parameter family of orbifold domains. Each distinct embedding of a 2223 stellate orbifold into the $\star 246$ tiling of \mathbb{H}^2 leads to a distinct embedded free tiling of \mathbb{H}^2 , following the prescription for tile edges given in Fig. 6. To fix the 2223 coverings relative to the $\star 246$ discre-

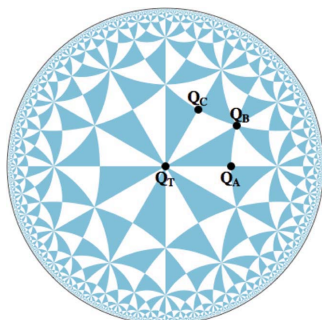


Figure 38
The locations of the reference frame generators of the 2223 symmetry group in the $\star 246$ tiling of \mathbb{H}^2 .

tization, we locate the basis set of generators, Q_T , Q_A , Q_B and Q_C as shown in Fig. 38. Note that the full fundamental domain of the stellate orbifold, characterized by the vertices Q'_T , Q'_A , Q'_B and Q'_C , which is required to form the complete Delaney–Dress representation of the abstract tilings, may be obtained by doubling the quadrilateral joining the generators across the line joining Q'_T and Q'_C .

APPENDIX B

Subgroups of $\star 246$ and $\star 2226$

See Tables 6 and 7.

We thank Stuart Ramsden for helpful discussions on many aspects of this work. MEE thanks the Humboldt Foundation for generous support.

References

- Adams, C. C. (2004). *The Knot Book: an Elementary Introduction to the Mathematical Theory of Knots*. Providence: American Mathematical Society.
- Alexandrov, E. V., Blatov, V. A., Kochetkov, A. V. & Proserpio, D. M. (2011). *CrystEngComm*, **13**, 3947–3958.
- Alexandrov, E. V., Blatov, V. A. & Proserpio, D. M. (2012). *Acta Cryst.* **A68**, 484–493.
- Baburin, I. A., Blatov, V. A., Carlucci, L., Ciani, G. & Proserpio, D. M. (2005). *J. Solid State Chem.* **178**, 2452–2474.
- Batten, S. & Robson, R. (1998). *Angew. Chem. Int. Ed. Engl.* **37**, 1461–1494.
- Beardon, A. F. (1995). *The Geometry of Discrete Groups*. New York: Springer-Verlag Inc.
- Beukemann, A. & Klee, W. (1992). *Z. Kristallogr.* **201**, 37–51.
- Blatov, V. A. (2006). *IUCr CompComm. Newsl.* **7**, 4–38.
- Blatov, V., Carlucci, L., Ciani, G. & Proserpio, D. (2004). *CrystEngComm*, **6**, 377–395.
- Blatov, V. A. & Proserpio, D. M. (2009). *Acta Cryst.* **A65**, 202–212.
- Cantarella, J., Kusner, R. B. & Sullivan, J. M. (2002). *Invent. Math.* **150**, 257–286.
- Carlucci, L., Ciani, G. & Proserpio, D. M. (2003). *Coord. Chem. Rev.* **246**, 247–289.
- Castle, T., Evans, M. & Hyde, S. T. (2008). *New J. Chem.* **32**, 1484–1492.
- Castle, T., Evans, M. & Hyde, S. (2011). *Prog. Theor. Phys. Suppl.* **191**, 235–244.
- Castle, T., Evans, M. E., Hyde, S. T., Ramsden, S. & Robins, V. (2012). *Interface Focus*, **2**, 555–566.

Table 6

Subgroups of $\star 246$ commensurate with the P , D and G minimal surfaces (Robins *et al.*, 2004a).

The group number, orbifold symbol, group index and the corresponding space groups on each of the P , D and G surfaces are given.

Group #	Orbifold	Index	P surface	D surface	G surface
129	$2\star 23$	2	$I432$	$Fd\bar{3}m$	$I4_132$
124	$\star 2223$	2	$Pm\bar{3}m$	$P4_232$	$I4_132$
123	$\star 2224$	3	$I4/mmm$	$P4_2/nmm$	$I4_1/acd$
122	$2\star 26$	4	$R\bar{3}m$	$R\bar{3}m$	$R\bar{3}c$
118	2223	4	$P432$	$F4_132$	$I4_132$
114	2224	6	$P4/nnc$	$I4_1/acd$	$I4_1/acd$
93	2226	8	$R\bar{3}c$	$R\bar{3}c$	$R\bar{3}c$

Table 7

Subgroups of $\star 2226$ commensurate with the H minimal surface (Robins *et al.*, 2004b).

The group number, orbifold symbol, group index and the corresponding space group on the H surface are given.

Group #	Orbifold	Index	H surface
32	$\star 2226$	1	$P6_3/mmc$
31	2226	2	$P\bar{3}1c$

- Chen, B., Eddaoudi, M., Hyde, S., O’Keeffe, M. & Yaghi, O. M. (2001). *Science*, **291**, 994–1021.
- Conway, J. (1992). *Groups, Combinatorics and Geometry*, Vol. 165 of *LMS Lecture Notes*, pp. 438–447. Cambridge University Press.
- Conway, J. H. & Huson, D. H. (2002). *Struct. Chem.* **13**, 247–257.
- Coxeter, H. S. M. (1947). *Non-Euclidean Geometry*. Toronto: University of Toronto Press.
- Coxeter, H. S. M. & Moser, W. O. J. (1972). *Generators and Relations for Discrete Groups*. Berlin: Springer-Verlag.
- Delgado-Friedrichs, O. (2001). *Discrete Comput. Geom.* **26**, 549–571.
- Delgado-Friedrichs, O. (2003). *Theor. Comput. Sci.* **303**, 431–445.
- Delgado-Friedrichs, O. (2012). *Generation, analysis and visualization of reticular ornaments using GAVROG*. <http://www.gavrog.com>.
- Delgado-Friedrichs, O. & Huson, D. (1999). *Discrete Comput. Geom.* **21**, 299–315.
- Delgado-Friedrichs, O. & O’Keeffe, M. (2003). *Acta Cryst.* **A59**, 351–360.
- Delgado Friedrichs, O., O’Keeffe, M. & Yaghi, O. M. (2003). *Acta Cryst.* **A59**, 22–27.
- Dress, A. W. M. (1987). *Adv. Math.* **63**, 196–212.
- Eon, J.-G. (2006). *Z. Kristallogr.* **221**, 93–98.
- Eon, J.-G., Proserpio, D. M. & Blatov, V. A. (2012). *Acta Cryst.* **A68**, 286–294.
- Evans, M. E. (2011). PhD thesis, Australian National University. <https://digitalcollections.anu.edu.au/handle/1885/9502>.
- Evans, M. E. & Hyde, S. T. (2011). *J. R. Soc. Interface*, **8**, 1274–1280.
- Evans, M. E., Robins, V. & Hyde, S. T. (2013). *Acta Cryst.* **A69**, 262–275.
- Fischer, W. & Koch, E. (1987). *Z. Kristallogr.* **179**, 31–52.
- Fogden, A. & Hyde, S. T. (1992). *Acta Cryst.* **A48**, 575–591.
- Han, Y., Zhang, D., Chng, L. L., Sun, J., Zhao, L., Zou, X. & Ying, J. Y. (2009). *Nat. Chem.* **1**, 123–127.
- Hilbert, D. & Cohn-Vossen, S. (1952). *Geometry and the Imagination*. New York: Chelsea Publishing Co.
- Huson, D. (1993). *Geom. Dedicata*, **47**, 269–296.
- Hyde, S. (1989). *Z. Kristallogr.* **187**, 165–186.
- Hyde, S., Andersson, S., Blum, Z., Lidin, S., Larsson, K., Landh, T. & Ninham, B. (1997). *The Language of Shape*. Amsterdam: Elsevier Science BV.

- Hyde, S. T., de Campo, L. & Oguey, C. (2009). *Soft Matter*, **5**, 2782–2794.
- Hyde, S. T. & Delgado-Friedrichs, O. (2011). *Solid State Sci.* **13**, 676–683.
- Hyde, S. T., Delgado-Friedrichs, O., Ramsden, S. J. & Robins, V. (2006). *Solid State Sci.* **8**, 740–752.
- Hyde, S. T., Larsson, A. K., Di Matteo, T., Ramsden, S. J. & Robins, V. (2003). *Aust. J. Chem.* **56**, 981–1000.
- Hyde, S. & Oguey, C. (2000). *Eur. Phys. J. B*, **16**, 613–630.
- Hyde, S. T. & Ramsden, S. J. (1999). *Chemical Topology: Applications and Techniques*, edited by D. Bonchev & D. Rouvray, *Mathematical Chemistry Series*, Vol. 6, pp. 35–174. New York: Gordon and Breach Science Publishers.
- Hyde, S. T. & Ramsden, S. (2000a). *Europhys. Lett.* **50**, 135–141.
- Hyde, S. T. & Ramsden, S. J. (2000b). *Discrete Mathematical Chemistry*, edited by P. Hansen, P. Fowler & M. Zheng, Vol. 51, *DIMACS Series in Discrete Mathematics and Theoretical Computer Science*, pp. 203–224. Amsterdam: American Mathematical Society.
- Hyde, S. T. & Ramsden, S. J. (2000c). *Europhys. Lett.* **50**, 135–141.
- Hyde, S. T. & Ramsden, S. J. (2003). *Eur. Phys. J. B*, **31**, 273–284.
- Hyde, S., Ramsden, S., Di Matteo, T. & Longdell, J. (2003). *Solid State Sci.* **5**, 35–45.
- Hyde, S. T., Ramsden, S. J. & Robins, V. (2013). In preparation.
- Hyde, S. T., Robins, V. & Ramsden, S. J. (2010). *Epinet*. <http://epinet.anu.edu.au>.
- Hyde, S. T. & Schröder-Turk, G. E. (2007). *Acta Cryst.* **A63**, 186–197.
- Kepert, C. J., Prior, T. J. & Rosseinsky, M. J. (2000). *J. Am. Chem. Soc.* **122**, 5158–5168.
- Klee, W. (2004). *Cryst. Res. Technol.* **39**, 959–968.
- Li, F., Clegg, J. K., Lindoy, L. F., Macquart, R. B. & Meehan, G. V. (2011). *Nat. Commun.* **2**, 205.
- Lindsay, J. (1959). *Am. Math. Monthly*, **16**, 117–118.
- Molnar, E. (2002). *Struct. Chem.* **13**, 267–275.
- Ockwig, N. W., Delgado-Friedrichs, O., O’Keeffe, M. & Yaghi, O. M. (2005). *Acc. Chem. Res.* **38**, 176–182.
- O’Keeffe, M., Eddaoudi, M., Li, H., Reineke, T. & Yaghi, O. M. (2000). *J. Solid State Chem.* **152**, 3–20.
- O’Keeffe, M., Peskov, M. A., Ramsden, S. J. & Yaghi, O. (2008). *Acc. Chem. Res.* **41**, 1782–1789.
- Pieranski, P. (1998). *Ideal Knots*, edited by A. Stasiak, V. Katritch & L. H. Kauffman, *Series on Knots and Everything*, Vol. 19, pp. 20–41. World Scientific.
- Ramsden, S. J., Robins, V. & Hyde, S. T. (2009). *Acta Cryst.* **A65**, 81–108.
- Reineke, T. M., Eddaoudi, M., Moler, D., O’Keeffe, M. & Yaghi, O. M. (2000). *J. Am. Chem. Soc.* **122**, 4843–4844.
- Robins, V., Ramsden, S. J. & Hyde, S. T. (2004a). *Eur. Phys. J. B*, **39**, 365–375.
- Robins, V., Ramsden, S. J. & Hyde, S. T. (2004b). *Physica A*, **339**, 173–180.
- Robins, V., Ramsden, S. J. & Hyde, S. T. (2005). *Eur. Phys. J. B*, **48**, 107–111.
- Sadoc, J.-F. & Charvolin, J. (1989). *Acta Cryst.* **A45**, 10–20.
- Schoen, A. H. (1970). *NASA Technical Note* TN D-5541.
- Schröder-Turk, G. E., de Campo, L., Evans, M. E., Saba, M., Kapfer, S., Varslot, T., Grosse-Brauckmann, K., Ramsden, S. J. & Hyde, S. T. (2013). *Faraday Discuss.* **161**, 215–247.
- Stasiak, A., Dubochet, J., Katritch, V. & Pieranski, P. (1998). *Ideal Knots*, edited by A. Stasiak, V. Katritch & L. H. Kauffman, *Series on Knots and Everything*, Vol. 19, pp. 1–19. World Scientific.
- Thurston, W. (1980). *The Geometry and Topology of Three-Manifolds*. Princeton University Press.
- Wells, A. (1977). *Three-dimensional Nets and Polyhedra*. New York: John Wiley and Sons.
- Wu, H., Yang, J., Su, Z.-M., Batten, S. R. & Ma, J.-F. (2011). *J. Am. Chem. Soc.* **133**, 11406–11409.